UTTAC-76, 2007
ISSN 1880-4748

ANNUAL REPORT

2006

TANDEM ACCELERATOR COMPLEX

Research Facility Center for Science and Technology
University of Tsukuba

http://www.tac.tsukuba.ac.jp/

UTTAC-76, 2007

UTTAC

ANNUAL REPORT 2006

TANDEM ACCELERATOR COMPLEX
Research Facility Center for Science and Technology
University of Tsukuba

http://www.tac.tsukuba.ac.jp/

UTTAC

ANNUAL REPORT 2006

April 1, 2006 – March 31, 2007

UTTAC-76 2007

Executive Editors: Yasuo Nagashima
Editors: Tetsuro Komatsubara, Kimikazu Sasa, Yoshihiro Yamato

Cover photo: Autumn at UTTAC.

UTTAC is a series of issues, which include annual reports of
Tandem Accelerator Complex, Research Facility Center
for Science and Technology, University of Tsukuba.
The issues may also include irregular reports written by English.

Tandem Accelerator Complex, Research Facility Center for Science and Technology,
University of Tsukuba
Tennodai 1-1-1, Tsukuba, Ibaraki 305-8577, Japan

http://www.tac.tsukuba.ac.jp/
annual@tac.tsukuba.ac.jp

PREFACE

During the academic year 2006, from April 2006 to March 2007, efforts have been paid to the stable operation both of 12UD Pelletron and 1MV Tandetron as well as to the construction of new beam lines. The new line for a μ-beam PIXE analysis has been thrown into research works as a new service. Several PIXE measurements such as fluid inclusions in quartz or element analysis in human hairs have been commenced.

In the field of element analysis, the ^{36}Cl accelerator mass spectrometry, ^{36}Cl-AMS, has been intensively used as a tool for studying of the A-bomb peak in the groundwater sampled at the root of Mt. Fuji. The $^{36}Cl^-$ AMS made a contribution to assess the nuclear waste clearance level. A hydrogen analysis with p-p elastic-recoil coincidence method has been applied to the geological research. Both the AMS and the Hydrogen analysis have been applied to the many research fields. A study of nano-particle formation in H_2O-N_2 mixture gases has been commenced with 20 MeV proton beam. The Eu concentration in Eu-doped GaN has been estimated by Ruthford backscattering spectroscopy, RBS.

In atomic and condensed matter physics, the evolution of resonant coherent excitation of hydrogen-like ions has been observed with a 180° electron spectroscopy. Nano-scale and high aspect ratio patterns were created on the SiO_2 and TiO_2 substances with accelerated fast heavy ions.

In the field of nuclear physics, a search for the resonant state in p+Si at the (p,n) threshold energy was precisely performed. A ^{118}Sn(d,p) reaction was intensively studied to look for deuteron Coulomb stripping. As a non-accelerator study, a conversion electron Mössbauer study on γ-Fe_2O_3 epitaxial thin films was pursued.

The agreement for both an academic exchange and an exchange of students has been extended with the Department of Nuclear Physics, the China Institute of Atomic Energy (CIAE), China. In accordance with this agreement, the UTTAC accepted a Chinese graduate student until the beginning of December, 2006 and three scientists in October 2006. Five UTTAC persons including an officer and three technicians were sent to the CIAE for discussion and information gathering.

The UTTAC organized a symposium entitled “new evolution toward to the interdisciplinary usage of the heavy ion beams produced by a multi tandem accelerator system”. This symposium was sponsored by the KEK-Tsukuba university co-operative research project.

An undertaking proposal has been granted by the Ministry of Education, Culture and Sport of Japan as a five year project starting from April 1st, 2007. The total budget of the project is predetermined ~300 million Yen and we are expecting this project might enforce the direction for a future of UTTAC.

Finally, Prof. H. Kudo has assumed office as a UTTAC director for the next year. Dr. Y. Aoki who was an effective user has retired. His contribution to the UTTAC is greatly acknowledged.

Yasuo Nagashima

Yasuo Nagashima
Director

CONTENTS

1. ACCELERATOR AND EXPERIMENTAL FACILITIES

2. NUCLEAR PHYSICS

3. ATOMIC AND SOLID STATE PHYSICS, AND CLUSTER SCIENCE

4. ION BEAM ANALYSIS AND APPLICATION

5. RELATED TOPICS

6. LIST OF PUBLICATIONS

1.

ACCELERATOR AND EXPERIMENTAL FACILITIES

1.1 Accelerator operation 2006

K. Sasa, S. Ishii, T. Takahashi, Y. Yamato, H. Kimura, H. Oshima, Y. Tajima, T. Komatsubara
and Y. Nagashima.

The 12UD Pelletron tandem accelerator

The total service time for the 12 UD Pelletron tandem accelerator users was 3,060 hours for the fiscal year 2006. During the service time, the accelerator operating time and the experimental beam time were 1875.1 and 1396.3 hours, respectively. The accelerator operating time was about 80 % relative to that in 2005. Fig.1 shows the accelerator operation hours per month. The beam time histogram with respect to the terminal voltage is shown in Fig.2. Fig.3 represents the percentage of the operation hours for the three ion sources and ion species. Fig.4 shows the percentage of the experimental beam time for the running research fields by the 12UD Pelletron tandem accelerator.

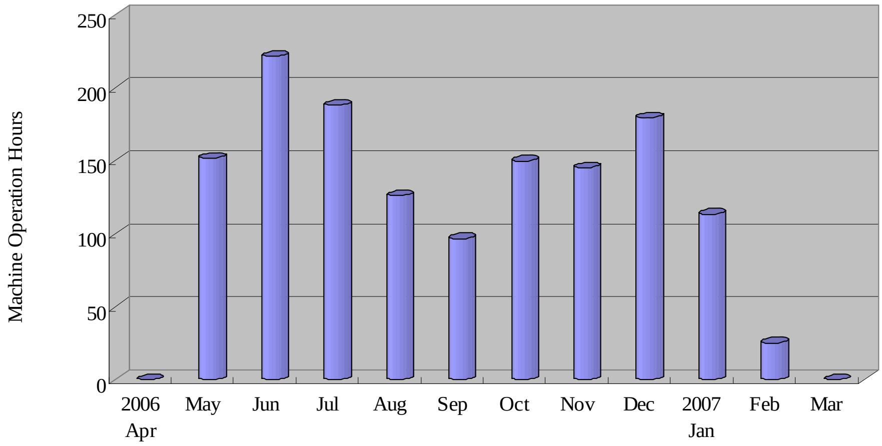

Fig.1. Accelerator operation hours per month for the fiscal year 2006.

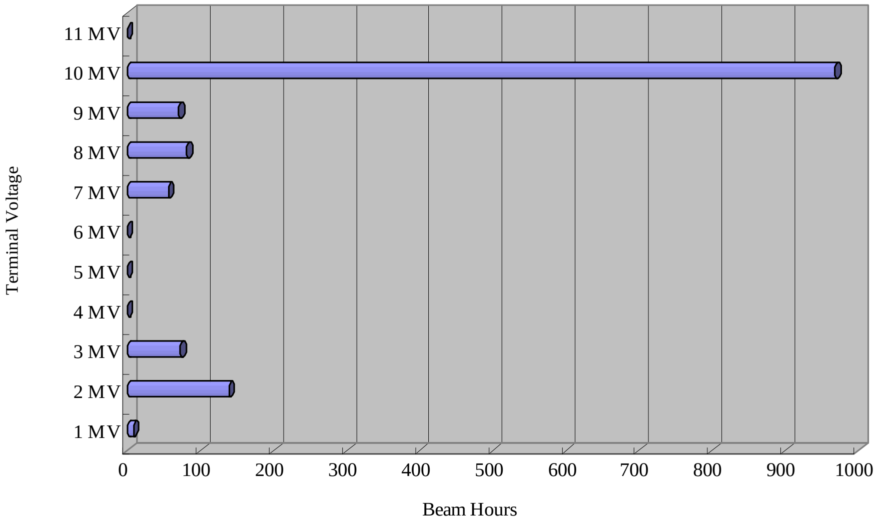

Fig.2. Beam time histogram as a function of the terminal voltage.

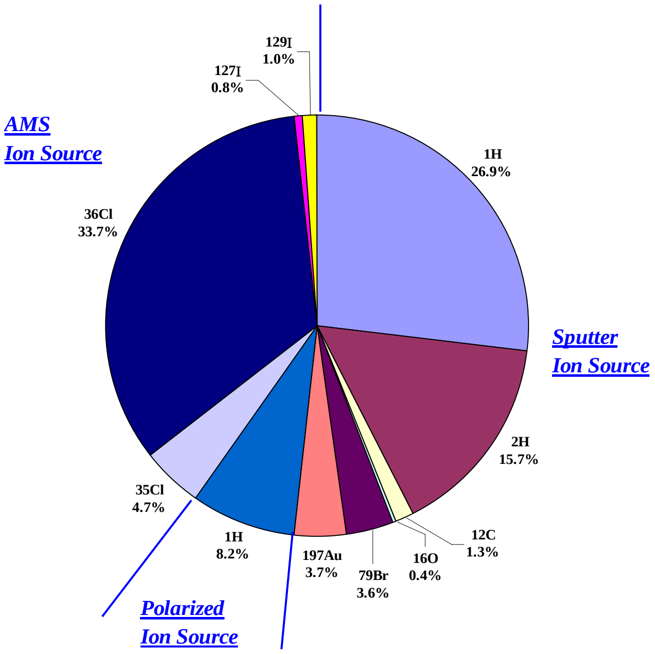

Fig.3. Percentage of the operation hours for the three ion sources and ion species.

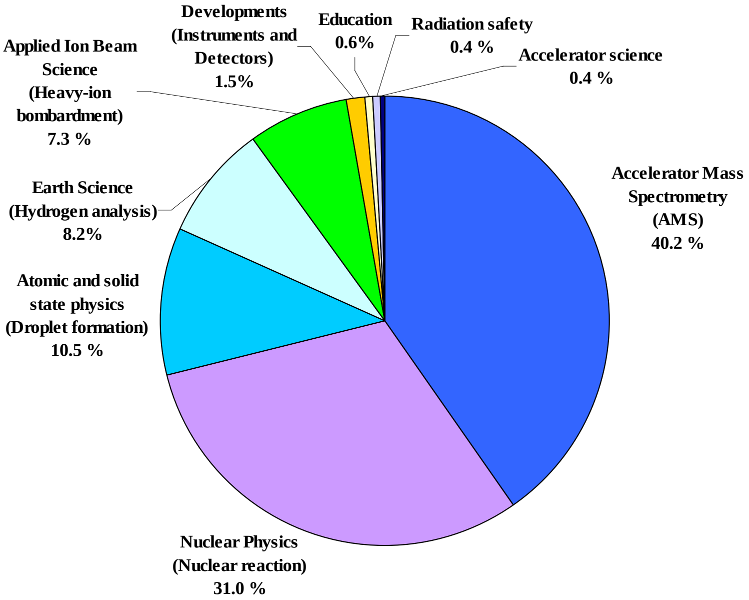

Fig.4. Percentage of the experimental beam time for the running research fields.

Because asbestos removal from the ion source floor and the SF_6 gas handling room was executed from February to March in 2007, the accelerator operating period was limited until January 2007. The scheduled maintenance in the spring 2007 was started on February 7. It was one month early compared with the normal schedule, therefore the accelerator operating period became one month shorter for the fiscal year 2006. The operating time at the terminal voltage of 10 MV accounted for nearly all of the beam time. The research field of the AMS study was the largest beam time ratio for the fiscal year 2006. Ion specie of ^{36}Cl for the AMS study was used the most with respect to operating hours.

In the year of 2006, we had some troubles with the SF_6 gas handling system by reason of deterioration of the overage facility, especially problems occurred to the gas compressor system. When the transportation of the SF_6 gas, cooling pure water was leaked from the cooling pipe in the gas compressor and flowed into the accelerator tank and the SF_6 gas storage tanks. The SF_6 gas handing system is under repair.

The 1MV Tandetron accelerator

The total service time for the 1 MV Tandetron accelerator users was 1,680 hours for the fiscal year 2006. The accelerator operating time and the experimental beam time were 652.4 and 289.0 hours, respectively. The accelerator operating time was about 187 % relative to that in 2005. Fig. 5 shows the percentage of accelerated ions with the 1MV Tandetron accelerator. Fig.6 shows the percentage of the experimental beam time for the running research fields. The main research fields of the 1MV Tandetron accelerator were the cluster physics, particle induced X-ray emission (PIXE) and Rutherford backscattering spectroscopy (RBS). The 1 MV Tandetron accelerator was also used for learning by experience about the accelerator science mainly for high school students and undergraduates.

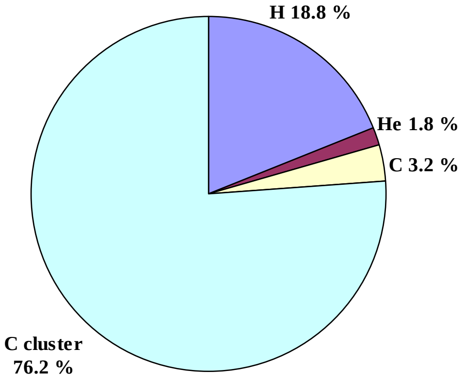

Fig.5. Percentage of accelerated ions with the 1MV Tandetron accelerator.

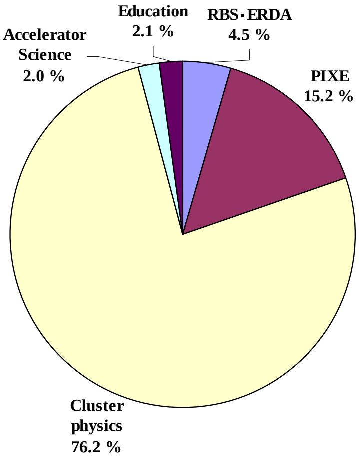

Fig.6. Percentage of the experimental beam time for the running research fields with the 1MV Tandetron accelerator.

2.

NUCLEAR PHYSICS

2.1 CDCC analysis of Oppenheimer-Phillips process

Y. Aoki, M.Iijima, T. Ishikawa, D. Inomata and N. Okumura [1]

After Lawrence et al.,[1] reported that the energy dependence of low energy deuteron induced reaction cross section is moderate than predicted by Gamow theory, Oppenheimer and Phillips[2] explained this energy dependence is due to Coulomb break up of incident deuteron followed by a liberated neutron capture.

We expect that the Coulomb break up process should accurately be described by continuum discretized coupled channels(CDCC)[3] analysis and neutron absorption cross section can be estimated by the expectation value of the imaginary part of the neutron optical potential. Based on this idea, we evaluated the following quantity for the process, we name OP process hereafter,

$$\sigma^C(d,p) = -\frac{\pi}{(2I_0+1)K_0^3}\sum_{JL_0}(2J+1)\sum_{jL_j}\left(\left|\chi^{jJ}_{L_jL_0}\right|^2 \frac{2\mu_R}{\hbar^2}W^n_{jj}\right)_{\mathbf{R}}. \tag{1}$$

In this expression I_0 and K_0 are spin and wave number of incident deuterons, $\chi^{jJ}_{L_jL_0}$ represent the center of mass motion of the beak up 'deuteron' with the incident and exit channel orbital angular momenta L_0 and L_j and W^n_{jj} stands for the matrix element of imaginary part of the neutron optical potential sandwiched by the scattering state wave function of p-n system, whose quantum number is collectively labeled "j". Because scattering state wave function extends out to infinity, matrix elements W^n_{jj} stretches out more than the imaginary potential itself, i.e., weak energy dependence of neutron capture cross section is expected.

Reid soft core potential[4] was used to generate deuteron bound state and scattering states of ${}^3S_1$-${}^3D_1$, ${}^3D_2$, ${}^3P_{0,1}$ and ${}^3P_2$-${}^3F_2$. Gaussian potential[3], which reproduce phase shift of ${}^3D_3$ state, was also used. Nucleon optical potential at half the deuteron kinetic energy of CH89[5] was used as the interaction between target and nucleons in the incident deuteron.

^{118}Sn(d,p) reaction is taken as a sample reaction. Figure 1 shows the energy dependence of neutron absorption cross section evaluated by using eq. (1). To study the role of Coulomb break up, off diagonal Coulomb matrix element is neglected, $\chi^{jJ}_{L_jL_0}$ are reevaluated and $\sigma^C(d,p)$ is also evaluated, i.e., pure nuclear break up followed by a neutron capture. Importance of Coulomb break up process can clearly be seen in the figure. Differential cross sections of $2s_{1/2}$ neutron transfer to form the ground state in ^{119}Sn are evaluated by using zero range DWBA program. Angle integrated values are also plotted in the figure to compare the energy dependence. Absolute values of the zero-range DWBA line is normalized to that of "no CBU" at $E_d = 10$ MeV. If we were to fit these energy dependence by $\exp(-2\pi\eta)/E^N$, N=10 for "with CBU" and N=6-7 for the rest of the lines.

Binding energy dependence of the "deuteron" should be one of the key parameter of the OP process. Potential depths of ${}^3S_1$-${}^3D_1$ states, i.e., central, spin orbit and tensor potentials of Reid [4] are scaled to generate wave functions of the bound and scattering states of ${}^3S_1$-${}^3D_1$. Fig. 2 shows this scaling parameter dependence of the virtual "deuteron".

Two reactions are studied, (1) binding energy dependence of OP cross sections of ^{118}Sn(d,p) reaction at $E_{``d''} = 5$ MeV and (2) incident energy dependence of ^{40}Ca($''d''$,p) reaction for BE("d")=0.1 MeV and

---

[1] Nagano National College of Technology

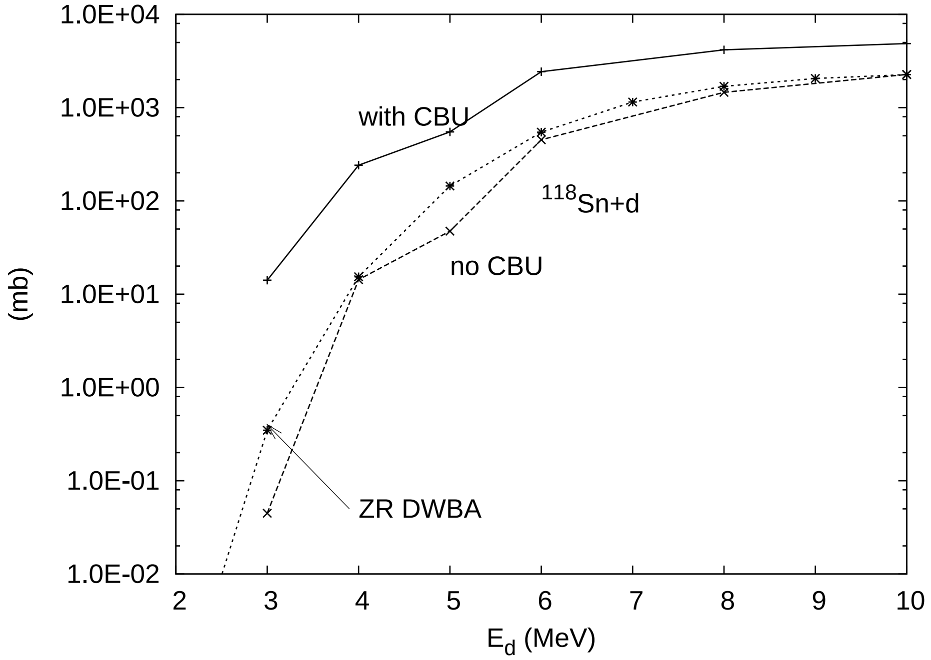

Fig. 1. Energy dependence of neutron absorption cross sections. Solid line, labeled “with CBU”, corresponds to that with Coulomb break up. Only nuclear break up is taken into account to draw thick dashed line, which is labeled “no CBU”. Thin dashed line is for zero-range DWBA calculation.

$E_{“d”}$=0.5 to 2 MeV. Fig. 3 shows the binding energy dependence of the former case.

Fig. 4 shows the incident energy dependence of virtual “deuteron” induced ^{40}Ca(“d”,p) reaction. Because binding energy is very low and Coulomb interaction is not very strong as that of the Sn target, nuclear break up contribution is stronger than that of Coulomb potential. The two contributions interfere destructively. Two lowest energy points can be fit by using $\sigma(BU) \propto \exp(-2\pi\eta)/E^{1.86}$. If the corresponding data, evaluated by replacing $\chi^{jJ}_{L_jL_0}$ by that of “deuteron” ground state, exponent reduces to 1.14, i.e., $\sigma(GS) \propto \exp(-2\pi\eta)/E^{1.14}$. This means that the incident energy of 0.5 to 0.75 MeV is roughly low enough to use the Gamow approximation. Even in this incident energy, energy dependence of OP process is not so steep as the Gamow prediction.

References

[1] Ernest O. Lawrence, Edwin McMillan and R.L. Thornton, Phys. Rev., **48**, 494(1935).

[2] J.R. Oppenheimer and M. Phillips, Phys. Rev., **48**, 500(1935).

[3] M. Kamimura, M. Yahiro, Y. Iseri, Y. Sakuragi, H. Kameyama and M. Kawai, Prog. Theo. Phys. Jpn. **89**,1(1986).

[4] R.V. Reid, Jr., Ann. Phys. **40**, 411(1968).

[5] R.L. Varner, Phys. Rep. **201**, 59(1991).

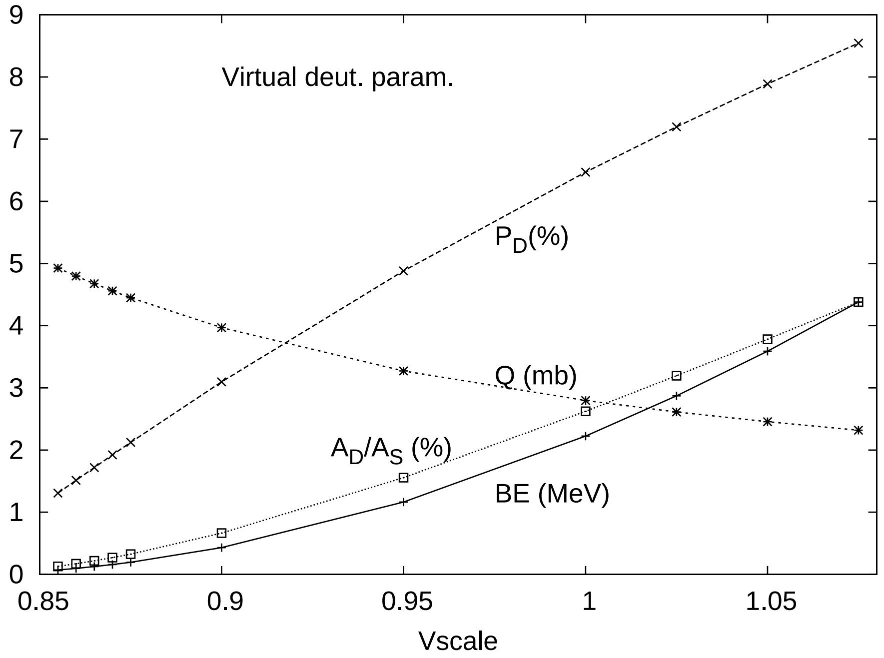

Fig. 2. Scaling factor dependence of the deuteron parameters. $P_d(\%)$ for D-state probability in percent, $Q(mb)$ for electric quadrupole moment in millibarn, $A_D/A_s(\times 100)$ for asymptotic ratio multiplied by 100 and $BE(MeV)$ for binding energy in MeV. Electric quadrupole moment increases when binding energy is decreased.

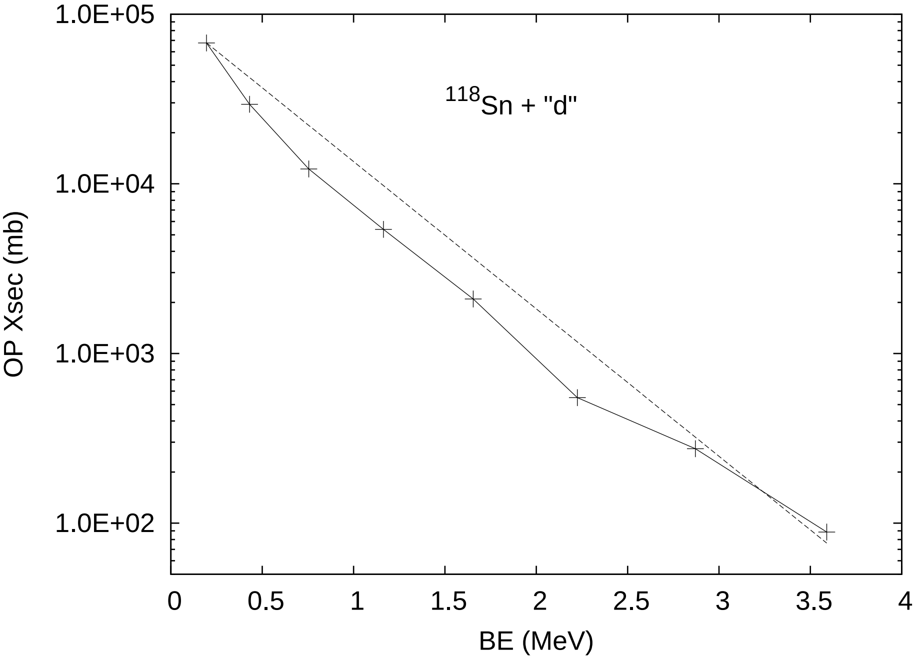

Fig. 3. Binding energy dependence of OP cross sections in ^{118}Sn(d,p) reaction. OP cross section σ increases exponentially with decreasing binding energy BE[MeV] as $\sigma \propto \exp\{-2 \times (BE)\}$.

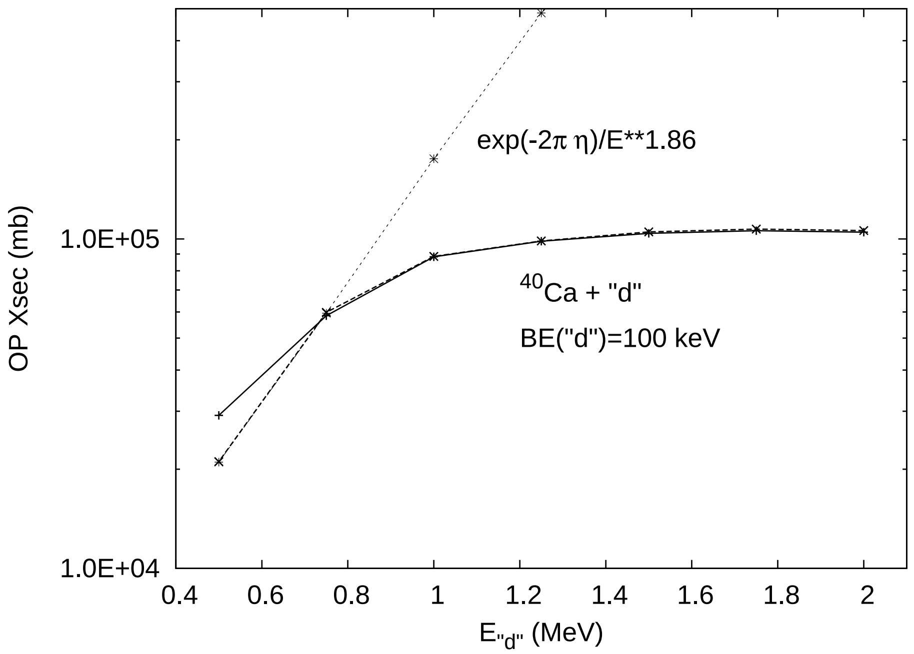

Fig. 4. Incident energy dependence of OP cross sections in ^{40}Ca("d",p) reaction. Binding energy of the virtual "deuteron" is 100 keV. Two lines, "with CBU" and "no CBU" overlap except for $E_{``d''} = 0.5$ MeV, where "with CBU" point is located at about half way for "no CBU" point.

2.2 Resonance search in ^{28}Si+p system around (p,n) threshold

Y. Aoki, M.Iijima, D. Inomata, T. Ishikawa, Y. Tagishi and N. Okumura [1]

Proton elastic scattering experiment was performed on ^{nat} Si target to study if resonance like behavior can be seen near the (p,n) threshold. Important experimental trait can be explained as follows, see fig. 1. We used 100 μm thick target and observed momentum spectrum of elastic protons at backward angles, typically 135°. Due to the energy losses through the thick target, momenta of elastic protons reflect the proton energy at the elastic scattering really take place. As is shown in the figure, energy of the elastically scattered protons which leave the target range from 14.31 to 12.90 MeV. Energy range of 0.56 MeV of the incident energy is expanded by the energy loss after elastic scattering. By measuring relative intensities of this elastic protons, we can measure the “excitation curve” of $15.64 \leq E_p \leq 16.2$ MeV by a single measurement.

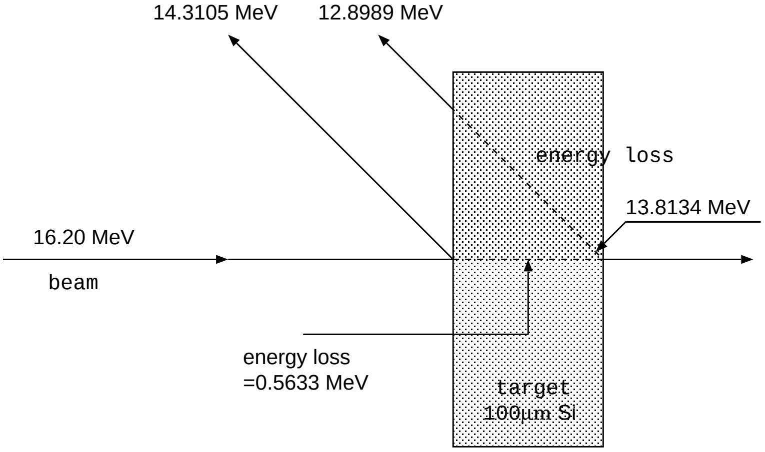

Fig. 1. Details of proton energy loss during the elastic scattering in the thick target. Protons of $E_p = 16.2$ MeV impinge onto the target and loose energy of 0.56 MeV during the passage through the target. Some tiny fraction of the protons are elastically scattered by 135°, depositing the kinetic energy and leave the target.

Target thickness was adjusted so that the maximum kinetic energy of inelastically scattered protons is less than the least kinetic energy of the elastic protons. Momentum analysis of ejectile protons are made by using a magnetic spectrograph, ESP90[1]. Protons are detected by a position sensitive proportional counter[2], which are backed by another proportional veto counter. Typical spectrum is shown in fig. 2.

Incident energy was changed from 19 to 14.5 MeV by about 300 keV step to make superposition of the ejectile spectrum easily. Fig. 3 shows the double differential cross sections thus obtained.

Many structure can be seen in the figure. Presence of threshold anomaly can be suggested by this figure. Polarized proton beam from Lamb shift type ion source[3] was used and vector analyzing power A_y was measured. Quench ratio method was used to measure the beam polarization. Fig. 4 shows the A_y at $\theta_{lab} = 135°$. A little improved energy resolution is realized. A small peak, which corresponds to the (p,n) threshold can clearly be seen.

---

[1] Nagano National College of Technology

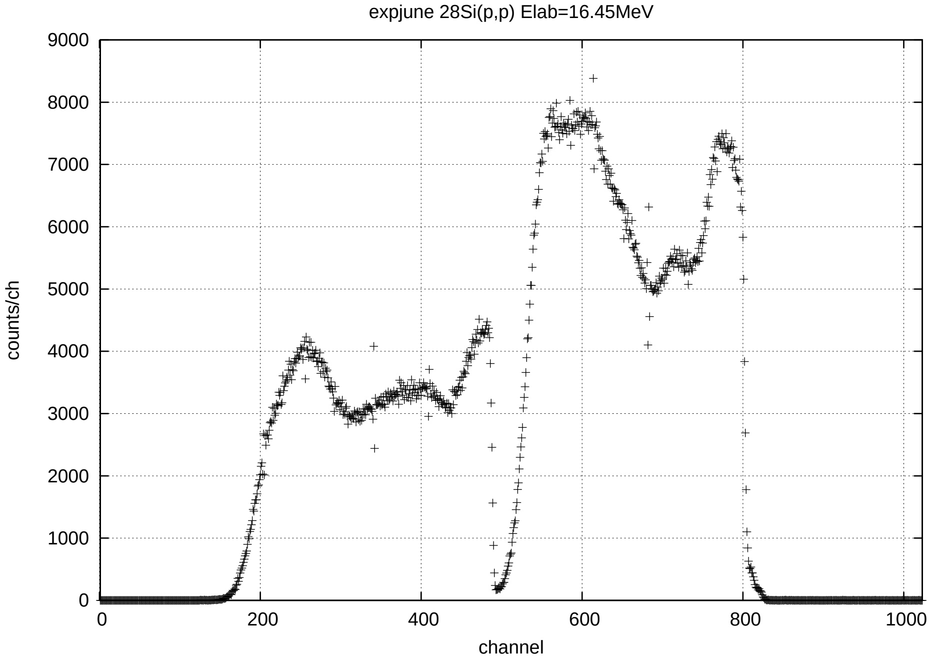

Fig. 2. Typical momentum spectrum for $E_p = 16.45$ MeV. A broad peak located around 500 to 800 channels correspond to elastic scattering, while the one at 200 to 500 channels for inelastic scattering leading to the 2_1^+ state in ^{28}Si. Intensities of elastic protons from ^{29,30}Si are very small and can only be identified by magnifying the figure and are neglected in the following analyses.

In summary, an anomaly can be identified at the (p,n) threshold energy. There are many structure in the double differential cross section and A_y curve, however. It is difficult to conclude there is a definite threshold anomaly.

References

[1] J.E. Spencer and H.A. Enge, Nucl. Instr. Meth., **49**, 181(1967).

[2] H. Iida, Y. Aoki, K. Yagi and M. Matoba, Nucl. Instr. Meth., **224**, 432(1984).

[3] Y. Tagishi and J. Sanada, Nucl. Instr. Meth., **164**, 411(1979).

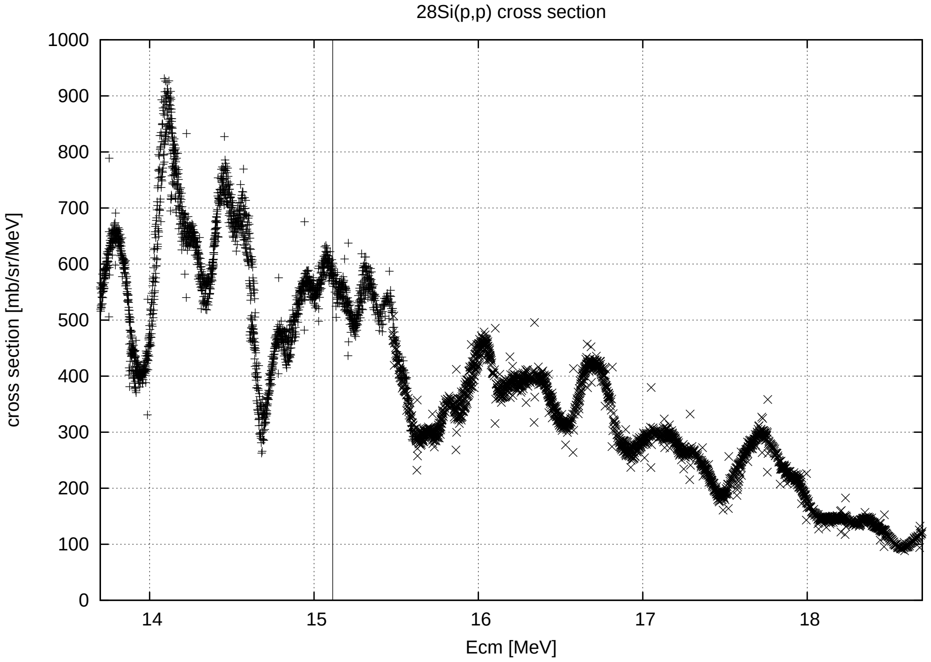

Fig. 3. Double differential cross section of elastic scattering of^{28}Si+p system at $\theta_{lab} = 135°$. Threshold energy of neutron knock on reaction is indicated by a solid line at 15.1 MeV.

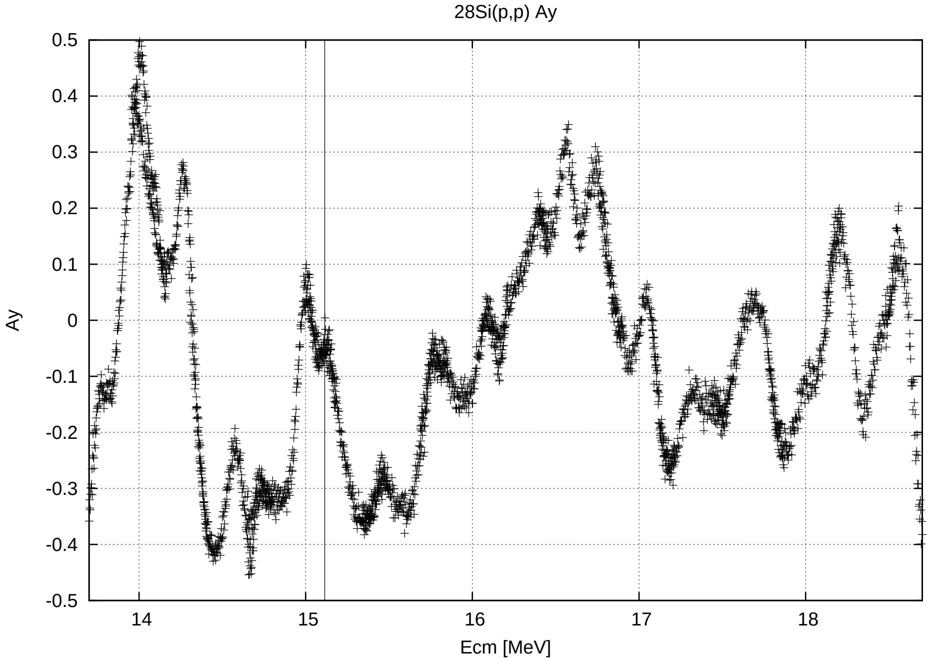

Fig. 4. Energy dependence of vector analyzing power A_y in elastic scattering of $^{28}Si + p$. Solid vertical line indicates the (p,n) threshold energy.

2.3 ^{118}Sn(d,p) reaction in search for Coulomb stripping of deuteron. IV

M.Iijima, T.Ishikawa, D.Inomata and Y.Aoki

The idea of Coulomb stripping was proposed by Oppenheimer and Phillips [1] in the 1930s. They thought that a neutron was absorbed following a Coulomb break-up of a deuteron. Later in the 1990s Bencze and Chandler [2] showed that the Oppenheimer-Phillips process produces negligible effect on the cross sections. Aoki [3] recently calculated total reaction cross sections by solving CDCC equation. The calculations were carried out with and without the Coulomb break-up contributions. It suggested Coulomb stripping was probable with a target of a large atomic number and the incident energy considerably lower than the Coulomb barrier.

We thought that reactions of $\Delta l = 0$ transfer would be preferred at sub-Coulomb energy and chose ^{118}Sn as a target, whose recoiled nucleus ^{119}Sn has a ground state of $\mathrm{s}_{1/2}$. We measured energy dependence of the sum of the differential cross sections for $^{118}\mathrm{Sn(d,p)}$ reactions leading to the ground, the first (23.9 keV) and the second (89.5 keV) excited states of ^{119}Sn, because we could not separate these three levels.

In the experiment, deuteron beams from 12 UD Pelletron at University of Tsukuba Tandem Accelerator Complex (UTTAC) were used. The deuterons hit ^{118}Sn target and elastically scattered deuterons and (d,p) protons were momentum analyzed by a spectrograph ESP90. They were then detected by a position sensitive single wire proportional chamber (SWPC) placed on the focal plane.

We started the experiment at $E_{\mathrm{lab}} = 6.0\,\mathrm{MeV}$ and lowered it to $5, 4, \cdots\,\mathrm{MeV}$. We prepared self-supporting enriched ^{118}Sn targets and a target with Au backings. The self-supporting targets were used to determine $\frac{d\sigma}{d\Omega}$ for $^{118}\mathrm{Sn(d,p_{0,1,2})}$ reactions at $E_{\mathrm{lab}} = 6.0\,\mathrm{MeV}$. The target with Au backings was used to measure relative yields of $^{118}\mathrm{Sn(d,p_{0,1,2})}$ reactions at $E_{\mathrm{lab}} = 3.2 \sim 6.0\,\mathrm{MeV}$. Fig. 1 is a typical spectrum of protons taken with the SWPC at $E_{\mathrm{lab}} = 3.2\,\mathrm{MeV}$. The yields obtained between $E_{\mathrm{lab}} = 3.2 \sim 5.0\,\mathrm{MeV}$ were normalized to $\frac{d\sigma}{d\Omega}$ at $E_{\mathrm{lab}} = 6.0\,\mathrm{MeV}$.

Thus determined $\frac{d\sigma}{d\Omega}$ for the sum of the $^{118}\mathrm{Sn(d,p_{0,1,2})}$ reactions were plotted in Fig. 2. The curved line in Fig. 2 is zero-range DWBA calculations performed for the $^{118}\mathrm{Sn(d,p_0)}$ reaction. The DWBA values are normalized to the experiments at $E_{\mathrm{lab}} = 6.0\,\mathrm{MeV}$. The DWBA calculations show good agreements with experimental values at $E_{\mathrm{lab}} = 4.0$, 5.0MeV, whereas it underestimates cross sections at $E_{\mathrm{lab}} = 3.2$, 3.5MeV. That might be due to the effect of Coulomb stripping. We are planning to perform CDCC calculations and comparing them with experiments.

References

[1] J. R. Oppenheimer and M. Phillips, Phys. Rev. **48**, 500 (1935)

[2] Gy. Bencze and Colston Chandler, Phys. Rev. C **53**, 880 (1996)

[3] Y. Aoki et al., UTTAC Annual Report, **71**, 22(2003)

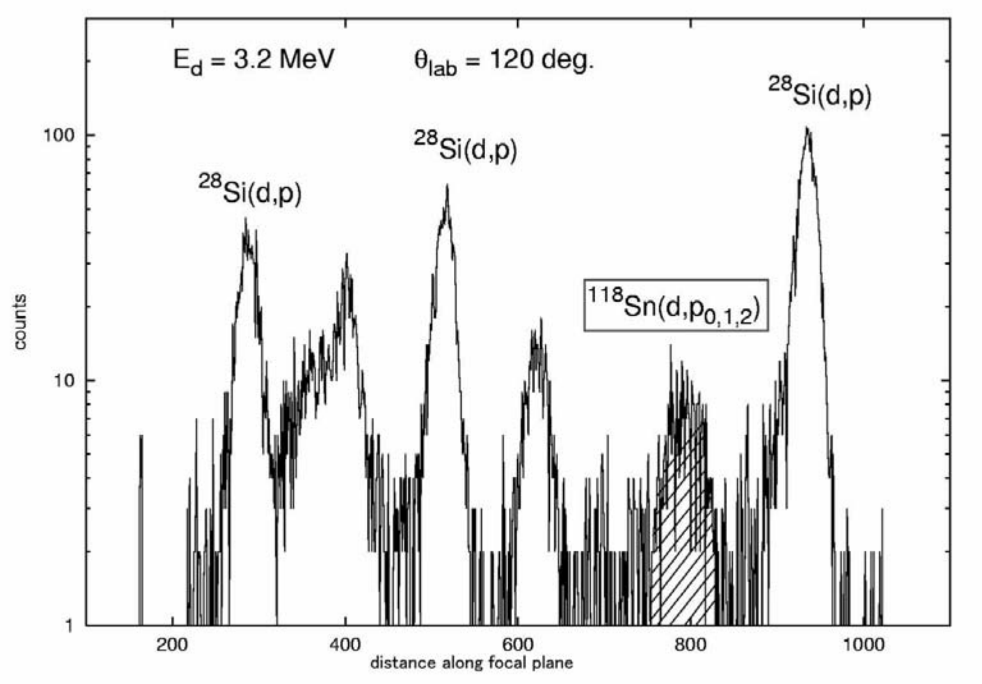

Fig. 1. A typical spectrum of protons

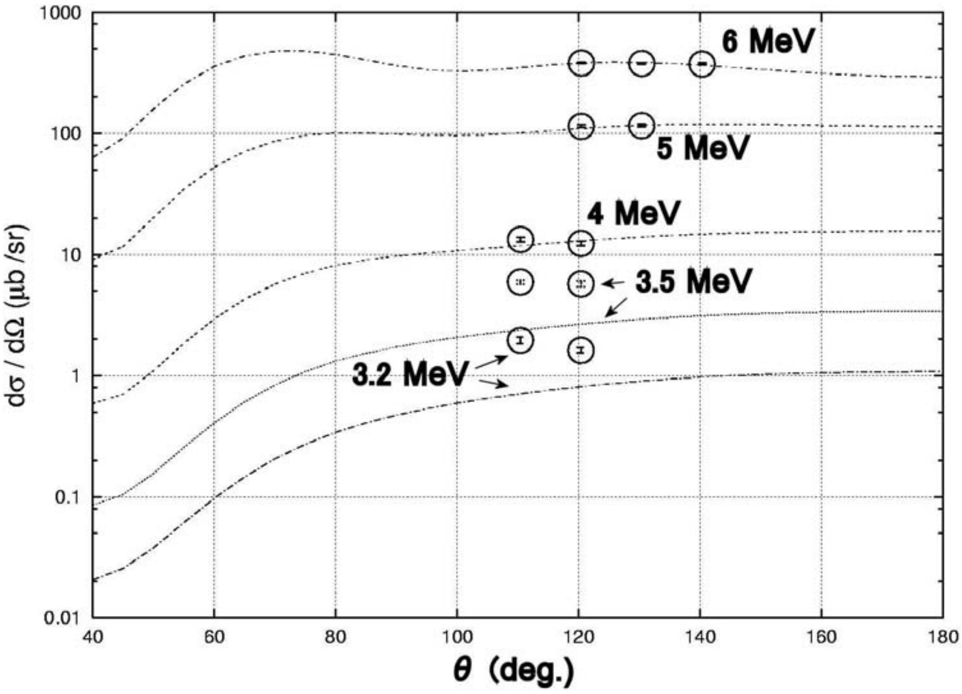

Fig. 2. $\frac{d\sigma}{d\Omega}$ and DWBA calculation

2.4 Measurement of the time response in Hybrid Photo Detector

T. Moriguchi, Y. Hashizume, T. Hoya, Y. Yasuda and A. Ozawa

The construction of the Isochronous Storage Ring is projected at RIKEN RI Beam Factory (RIBF) . The Storage Ring will be able to measure mass of RI to investigate the R-process path. To perform individual injection [1] , the Kicker magnet of the Ring should be excited by the trigger signal in the detectors in BigRIPS. Thus, the trigger signal which transit from the trigger detector to the Kicker magnet must be faster than the arrival of RI at the Kicker magnet. The prediction of the time of flight (TOF) is ~880ns for RI beam from the trigger detector to the Kicker magnet. On the other hand, the trigger signal, is ~850ns, considering the transmission time of the circuit and cable and rise time of the Kicker magnet except the transit time of the trigger detector. Here, we assumed to use a photo multi tube (PMT) that the transit time is generally ~30ns. Therefore, it is more desirable for the trigger detector to have the faster transit time. We also considered using the trigger detector as a TOF detector which needs a good time resolution.

A Hybrid Photo Detector (HPD) [2] has a fast transit time. Figure 1 shows a schematic view of the multiplication mechanism in HPD. The structure of HPD is that an Avalanche Photo Diode (APD) is included in the vacuum tube with a photo cathode. Photo-Electrons (PEs) which are emitted from a photo cathode are accelerated by 8.5kV high voltage. When accelerated PEs strike against APD, the kinetic energy of PEs is used for creating electron-hole pairs. This mechanism is called the bombarded gain (~10^3) . Created electrons cause an avalanche effect in APD with 150V bias voltage. This avalanche gain is about 50. So the total gain of HPD is ~10^4. Since this multiplication mechanism of HPD is different from the mechanism due to the multi dynodes like PMT, a transit time of HPD is fast. Figure 2 shows HPD (HAMAMATSU R7110U-07) that we used in this experiment.

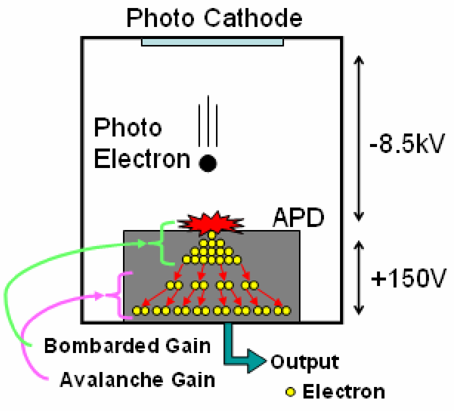

Fig.1. Schematic view of the multiplication mechanism in HPD.

Fig.2. HPD (HAMAMATSU R7110U-07) that we used in this experiment.

The experiment was performed at 1F course with Q-D-Q magnets in the 12UD tandem accelerator of UTTAC using 60MeV carbon beam. The beam intensity was 1nA. Figure 3 shows a schematic view of the experimental setup. HPD was connected to the plastic scintillator (BC408 50x50x0.6) . The another side of the scintillator was connected to PMT (HAMAMATSU R4998) in order to measure the differences of the transit time of both detectors. A 2μm Au foil was installed at the entrance of Q-D-Q to decrease the beam intensity. The intensity was 500cps at the scintillator. A coincidence signal between HPD and PMT was used as a trigger signal when we took data of the time resolution.

Figure 4 shows typical pulse shapes from two detectors without preamplifiers which was monitored by an oscilloscope. As shown in Fig.4, HPD signal is about 10ns faster than PMT. Since the pulse height of HPD was 1.5mV, we used preamplifiers (ORTEC AN302/N) and measured the time resolution of HPD. The typical time resolution of HPD was 664ps (σ) . It is noted that the time resolution of PMT was 137ps (σ) on using 17MeV proton beam [3] .

In summary, the transit time of HPD is faster than PMT and the time resolution of HPD is worse than PMT. In future, we will investigate to improve the time resolution of HPD.

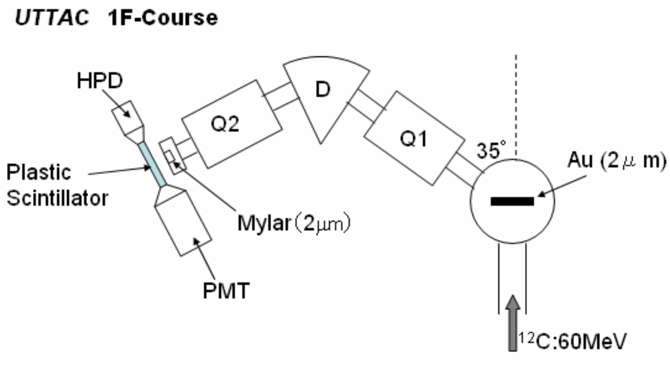

Fig.3. Schematic view of the experimental set up.

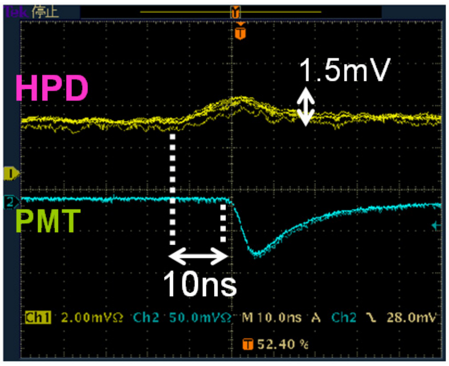

Fig.4. Typical pulse shapes which upper and lower are HPD and PMT, respectively.

References

[1] I. Meshkov *et al.*, Nucl. Instrum. Methods A **523** (2004) 262.

[2] M. Suyama *et al.*, IEEE Trans. Nucl. Sci. **44** (1997) 985.

[3] Y. Hashizume *et al.*, UTTAC Annual Report 2005, UTTAC-**75** (2006) 20.

2.5 Radiation damage study of PHENIX VTX Si sensor

J. Asai[1], R. Ichimiya[1], M. Kawashima,[2] T. Komatsubara, K. Kurita[2], K. Sakashita[3]

1 Introduction

Si vertex detector(VTX)[1] is currently under construction as an upgrade project for the RHIC-PHENIX experiment. Due to the high luminosity environment expected during the future runs, the radiation damage effect is of major concern. Among the several radiation damage effects, the amount of leakage current increase is the biggest problem for us. It is because our DC-coupled preamplifiers will saturate when the leakage current reaches 15nA/channel. Therefore, the main purpose of this experiment was to detemine the leakage current increase of the actual Si sensor after proton beam irradiation.

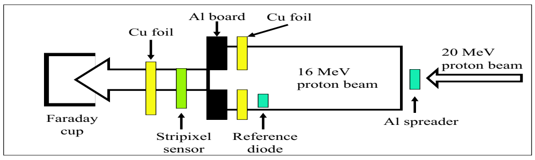

Fig. 1. Beam test setup with 16 MeV protons.

2 Beam irradiation test setup

In preparation for the tests, we designed a printed circuit board (PCB) for the stripixel sensor. Before the beam irradiation tests, stripixel sensors were mounted on the PCB and pre-irradiation leakage current measurements were done.

It is necessary to avoid localization in beam experiments to simulate almost uniform irradiation in the actual PHENIX environment. The setup of the 16 MeV proton irradiation test is shown in Fig. 1. The original 20 MeV proton beam from the Tandem Van de Graaff accelerator was spread with a 0.5 mm thick aluminum plate by Coulomb multiple scattering. The standard deviation of the spread was 3.8 cm at the sensor under test. The energy of the beam after the spreader was also affected and the mean value energy of the beam was 16 MeV. An aluminum collimator plate of 5 mm thickness was placed 150 cm downstream of the spreader. The Al collimator had a square opening of the size 30×30 mm^2 which was aligned to the center of the beam. A Cu foil was mounted in front of the collimator and it had the same opening so that the beam directly entered the stripixel sensor. The Al collimator size was 200×150 mm^2 to cover the PCB. One full stripixel pattern of the sensor was irradiated with 16 MeV proton spread beam through the opening of the collimator. A reference diode was placed by the side of the stripixel sensor on the front Cu foil. A Faraday cup was used for the beam fluence monitor at the end of the beam line. A magnetic field was applied to the cup to sweep away escaping secondary electrons.

---

[1] RIKEN

[2] Rikkyo University

[3] Tokyo Institute of Technology

3 Fluence determination

The fluence at the stripixel sensor position was estimated from the reference diode, which was irradiated together with the stripixel sensor. The estimation required a geometrical correction due to the Gaussian shape of the beam profile.

In order to measure the beam profile at the stripixel sensor, a plane Cu foil without a rectangular opening was irradiated at the same location as that of the test stripixel sensor. The proton beam had the same energy and the same intensity distribution. After the irradiation was over, the activated Cu foil (^{63}Zn*) was taken out from the chamber and was laid on an imaging plate (IP) to transfer the intensity map. The IP is a 2-dimensional radiation recording device, which can be read out by scanning laser stimulated luminescence. [2] The shape of the distribution was found to be consistent within a few percent with the calculated Coulomb multiple scattering.

We evaluated the average fluence for the whole stripixel sensor area using the measured distribution. The average fluence of the stripixel sensor was 93% of that of the beam center, while that of the reference diode was 73%. The fluence at the stripixel sensor was finally determined to be 2.4×10^{12} N_{eq}/cm^2 by taking into consideration the ratio of the average fluences measured and the hardness factor 3.0 for 16 MeV protons. This value was equivalent to 10 years of RHIC running. While the relative intensity of the activation was determined with the IP measurement, the absolute number of protons which irradiated the stripixel sensor was confirmed by the amount of the known γ ray intensities from the activated Cu foil.

4 Result

The increase of leakage current was estimated at 20°C. The current related damage rate α was determined from the temperature history recorded by a temperature logger, which was installed in the same setup. The increase of leakage current is defined as difference between the pre-irradiation and post-annealing leakage current at V_{FD} and T = 20°C. The annealing was done at 60°C for 80 minutes. The final measurement result was (74± 30%) nA/channel and it was found that we need to set the operation temperature of the Si sensors at least down to 0°C to reduce the actural leakage current. This information will be fed back to the design of the mounting sturucture and the cooling system of VTX.

References

[1] Z. Li, et al., Nucl. Instr.and Meth. A 518 (2004) 300-304, A 518 (2004) 738-753, A 535 (2004) 404-409, A 541 (2005) 137-143

[2] Sonoda M, Takano M, Migahara J, Kato H. Computed radiography utilizing scanning laser stimulated luminescence. Radiology. 1983;148:833-838.

3.

ATOMIC AND SOLID STATE PHYSICS,

AND

CLUSTER SCIENCE

3.1 Size of track potential in KCl studied with a cluster beam

H. Arai, S. Tomita, S. Ishii, K. Sasa and H. Kudo

Empirically, the yield of secondary electron by fast ion bomberdment is propotional to the electronic stopping power for conducting materials. For insulators, however, it is known that there is deviation from this relation. This could be due to so-called ”track potential” [1]. When fast ions impinge on insulating materials, electrons are scattered, and positively charged region is created. The positively charged region captures a part of the scattered electrons, and results in the reduction of secondary electron yield [2]. But there is only qualitative discussions on the problem, so far. More experimental observations are required to characterize the track potential. In present work, we investigated on the size of the track potential by using fast cluster ions.

When fast cluster ions are incident on insulator, a set of track potential fields is induced by individual atoms in the cluster. If the radius of track is larger than the distance between the cluster atoms, the potential fields overlap each other and become higher than for the case of single atom injection which, as a result, effectively reduce amount of secondary electrons. Therefore, by comparing the cluster-induced secondary electron yields from insulators and conductors, we can obtain infomation about the size of track potential.

Schematic drawing of the experimental setup is shown in Fig 1. Beams of carbon cluster ions were obtaned from the 1 MV Tandetron accelerator at UTTAC. The cluster ions from accelerator impinged on the target where a voltage of $V = -30$ V was applied. About 1 cm upstream from the target, a grounded plate was placed, so that the emitted electrons in the backward direction were accelerated and detected in an electron spectrometer. The spectrometer is a 45° parallel-plate electrostatic spectrometer of the double deflection type. The electrons were counted by a channeltron detector whose anode potential was set to 200 V to increase the detection efficiency of low energy electrons. To monitor the beam intensity, a beam chopper was placed just after aparture. The secondary electrons from the chopping electrode were detected with another channeltron. In the front of the channeltron, a grid electrode held at 100 V was placed so that only the electrons which have energies higher than 100 eV were detected. No vicinage effect is expected for such high-energy electron yield, therefore the electron yield is propotional to the beam intensity. The energy of the carbon clusters C_n^+ (n =1 to 4) was 0.5 MeV/atom. The targets used were KCl for insulator and highly oriented pyrolytic graphite (HOPG) for conductor which could not induce the track potential. The vacuum pressure was $\sim 3 \times 10^{-6}$ Pa during the beam irradiation.

The relative electron yield, i.e. the ratio of the yield per cluster to the yield for n=1 are shown in Fig.2 as a function of cluster size n. The result for HOPG reproduces the reduction of the yields from $Y_n/Y_1 = n$, as already reported [3]. If the track potentials overlap each other, the potential become higher than the case of single atom injection, and thereforethe additional reduction have to be observed for KCl. But there is no discernible difference between KCl and HOPG cases. From the present experiments, we conclude that the track potentials induced by the clusters do not have effective overlaps. These results indicate that the track potential radius is the same order to the interatomic distance ($\sim$ 1.3 Å) in the impinging clusters.

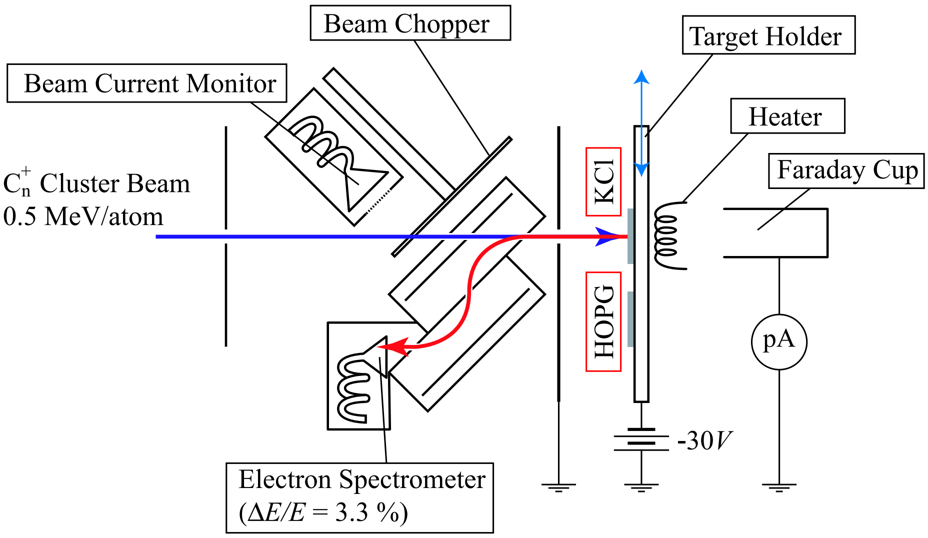

Fig. 1. Schematic drawing of the experimental setup.

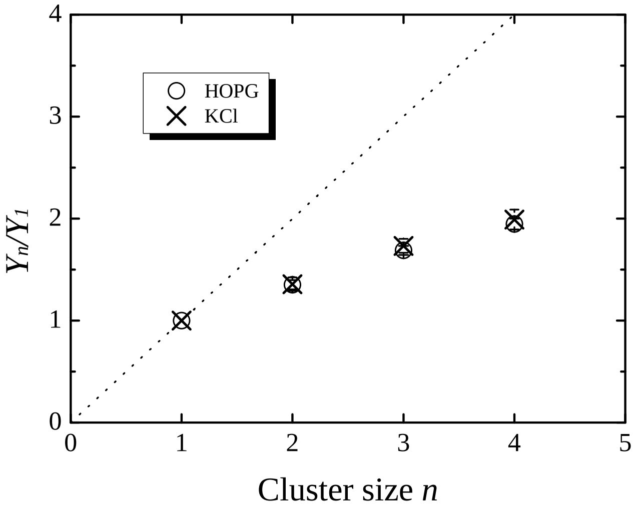

Fig. 2. Relative electron yield as a function of the cluster size n. Dotted line indicates $Y_n/Y_1 = n$.

References

[1] J. E. Borovsky et al., Phys. Rev. A **43**, 1433 (1991).

[2] K. Kimura et al., Nucl. Instrum. Methods Phys. Res. B **193**, 661 (2002).

[3] H. Kudo et al., Jpn. J. Appl. Phys. **45**, 565 (2006).

3.2 Nanoparticle formation in H_2O/N_2 mixtures under irradiation of 20 MeV protons

S. Kanda, M. Fujieda, M. Imanaka[1], K. Sasa, S. Tomita and H. Kudo

The strong correlation between the Earth's total low-altitude cloud cover and galactic cosmic ray flux is first reported in 1997 [1]. However, the mechanism of cloud production by galactic cosmic rays is not fully understood yet. One possible explanation is that atmospheric ions produced by galactic cosmic rays enhance the nucleation and early growth of ultrafine condensation nuclei from trace precursor vapors and water in the atmosphere. The ultrafine condensation nuclei eventually grow into the cloud condensation nuclei with about 100 nm diameter.

To study the ion-induced nucleation mechanism, we measured the size distribution of water droplet formed from humidified nitrogen by ion-induced nucleation. The ions were introduced either by irradiation of 20 MeV protons or by corona discharge. The experiments were conducted at the tandem accelerator, University of Tsukuba (UTTAC). The sizes of the droplets formed inside the humidified nitrogen were measured by a differential mobility analyzer (DMA).

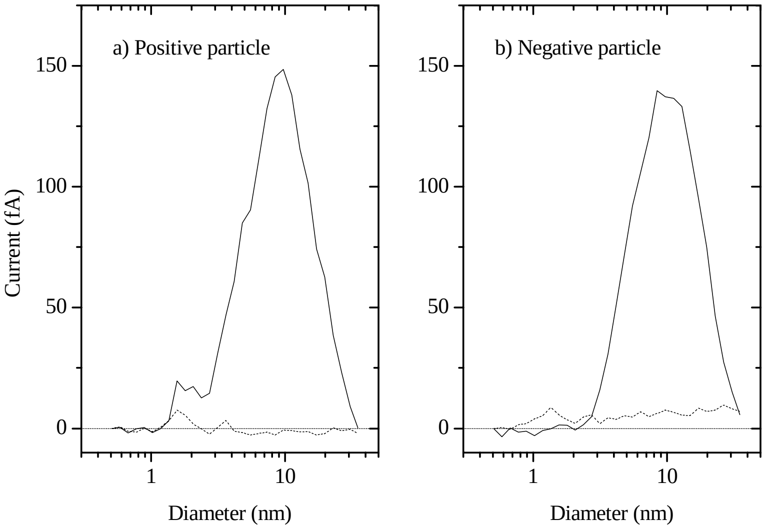

Fig. 1. Spectra of diameter of nanoparticles formed by irradiation of 20 MeV protons. The solid and dotted curves represent the spectra for humidified and dried nitrogen, respectively.

The size distributions of ion-induced droplets are shown in Fig. 1. Both positively and negatively charged droplets with diameter of about 10 nm are clearly observed only with humidified nitrogen, which confirm the production of water nanoparticles by ion nucleation. The yield of positive particle is almost

---

[1] RIKEN, Wako, Saitama, 351-0198, Japan

the same as that of negative particle.

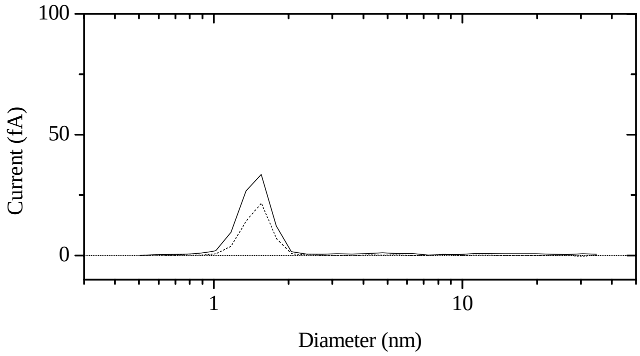

Fig. 2. Spectra of diameter of nanoparticle formed by corona discharge. The solid and dotted curves represent the humidified and dried cases, respectively. The humidity was 80 %. The discharge voltage was 8.4 kV.

On the other hand, the nanoparticles can not be observed with corona discharge (Fig. 2) except some peaks due to contamination.

The protons produce both positive and negative ions in a sample gas, while there are only positive ions when ionized by corona discharge. This fact implies importance of the presence of both positive and negative ions, which attract each other by coulomb interactions. As a result, the enhancement of collision probability allows the formation of 10 nm droplets.

References

[1] H. Svensmark and E. Friis-Christensen, J. Atoms. Solar Terr. Phys. 59,1225 (1997)

3.3 Vicinage effect on the energy loss of carbon clusters

M. Murakami, S. Tomita, T. Nishimura, S. Ishii, K. Sasa and H. Kudo

When fast molecular ions are incident on a solid, the energy loss per atom is different from that of single atomic ions. This is known as “vicinage effect” and first reported in 1974 for H_2^+[1]. The energy loss of H_2^+ is lower than that of equal-velocity H^+ at low injection energy, and becomes larger than H^+ at high energies. In 1992 Baudin *et al.* [5] performed similar experiments with fast carbon clusters and found higher energy loss is for clusters than atomic ions at high energies. The results are quantitatively understood by considering the interference of electrons scattered by individual atoms[2, 6]. According to the theoretical calculation, the energy loss of carbon cluster becomes lower at low injection energies like for the case of hydrogen molecule. But, this is not observed yet. Indeed, the reported data suffered large experimental errors more than 10%[3, 4]. More precise measurement is required.

The main causes of the large error bar are pulse height defect of solid state detector (SSD) which is expected to occur for fast C_n^+[7] and time fluctuations of electric devices. To improve the experimental quality, we introduced a new target device and used backscattering technique to measure the energy of ions transmitted through thin carbon foils. Fig.1 shows experimental set up. A thin carbon foil was mounted on one side of double frame which underwent metronomic motion together with other empty frame. The projectiles transmitted either through the foil or the empty frame hit thin Au target placed at just downstream of the device. The energy of the scattered carbon atoms by the target was measured with SSD at a backward angle, so that only carbon atom was detected. In this way, we avoid pulse height defect of SSD. The target device allowed almost simultaneous measurement with and without target, which canceled the fluctuations of electric devices.

In Fig.2, the results are shown together with theoretical predictions. There can be seen a slight but perceptible difference from atomic ion. The energy loss for cluster ions is lower than that of atomic ion at 0.5 MeV/atom, and agrees with theoretical values. The experimental error of the present data is estimated to be about ±1% which is much better than that of former experiments. The improved experimental methods enable us to perform more detailed comparison with theoretical calculations.

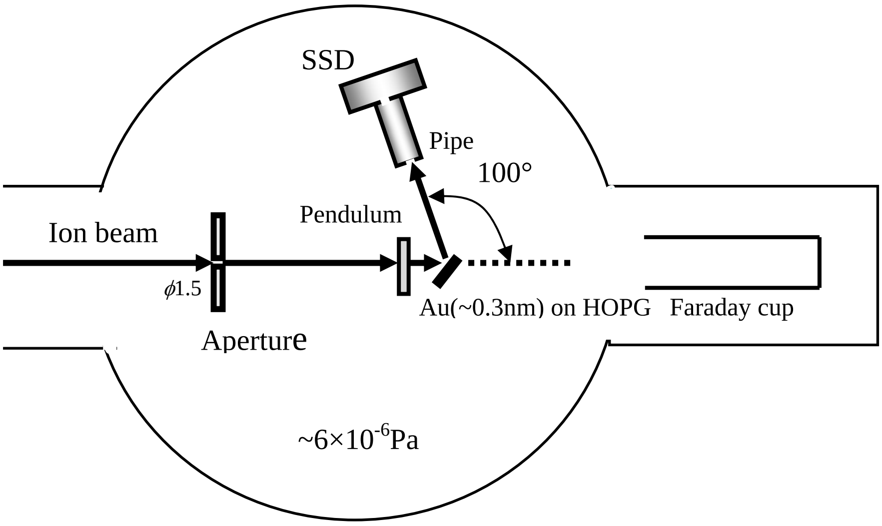

Fig. 1. Schematic view of the experimental setup in the scattering chamber.

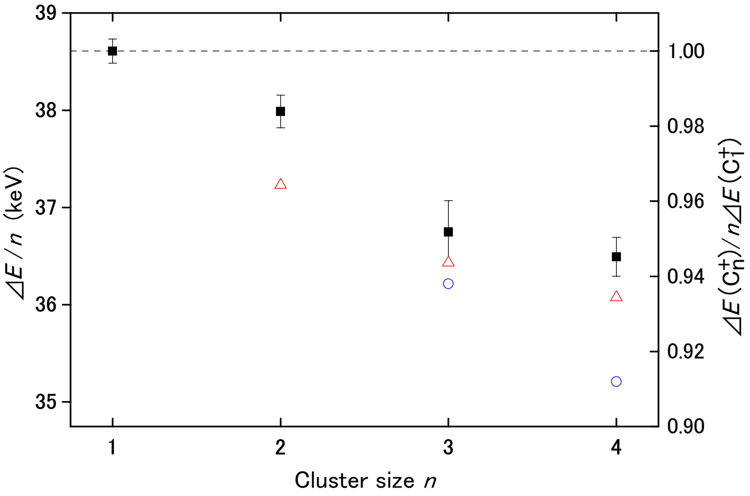

Fig. 2. Energy loss per atom of 0.5MeV/atom C_n^+ (circles) plotted together with theoretical prediction from Ref.[6] for ring (triangles) and linear structures (squares).

References

[1] W. Brandt, A. Ratkowski, and R.H. Ritchie, *Phys. Rev. Lett.* **33**, 1325 (1974)

[2] N.R. Arista, *Phys. Rev. B*, **18**, 1 (1978)

[3] K. Narumi *et al*, *Nucl. Instrum. Methods Phys. Res. B.* **135**, 77 (1998)

[4] C. Tomaschko *et al*, *Nucl. Instrum. Methods Phys. Res. B.* **103**, 407 (1995)

[5] K. Baudin *et al*, *Nucl. Instrum. Methods Phys. Res. B.* **94**, 341 (1994)

[6] T. Kaneko, *Phys. Rev. A.* **66**, 052901 (2002)

[7] M. Seidl, *et al*, *Nucl. Instrum. Methods Phys. Res. B.* **183**, 502 (2001)

3.4 The science of 3d transition-metal oxide system (2006–2007)

M. Onoda, T. Ikeda, K. Takao, Y. Kikuchi, A. Sasaki, W. Onoda, T. Maekoya, Y. Mizuguchi, I. Gotoh and S. Tsunegi

The structural and electronic properties of 3d transition-metal oxides and bronzes have been explored by means of x-ray four-circle diffraction and through measurements of magnetic resonance (NMR and ESR), magnetization, and electronic transport, in order to extract characteristic properties in the **quantum spin-fluctuation system**, **correlated electron system**, **electron-phonon-coupling system**, and **novel materials** such as **a new type of superconductors**, **composite crystals**, **thermoelectric devices** and **secondary ion batteries** [1, 2]. At the Tandem Accelerator Center, Varian continuous-wave and Bruker pulse NMR spectrometers have been used. This report describes briefly recent progress for the correlated electron system [1].

The structural and electronic properties of the triangular lattice system Na_xCoO_2 with nominal compositions of $0.7 \leq x \leq 1$ annealed at temperatures from 923 to 1123 K have been investigated. According to the annealing temperature, these properties for the single-phase specimens vary significantly, since the chemical composition as well as the local structure is modified. The overall temperature dependences of thermoelectric power are approximately explained with the two conduction path model and those of magnetic susceptibility at high temperatures are fitted with the Curie−Weiss law. The specimens annealed below T_{ac} that ranges from 973 to 1023 K have the enhanced gap for the poor metallic carriers and they are less magnetic having the Curie constant almost consistent with the localized electron model. On the other hand, above T_{ac}, the apparent gap of poor metallic carriers is reduced significantly and the Curie−Weiss parameters are enhanced, and the antiferromagnetic or spin density wave-like transition takes place. At this transition temperature, the resistivity becomes smaller than the value extrapolated from the high temperature side and the thermoelectric power exhibits a hump. This suggests that spin fluctuations are mainly responsible for the transport mechanism. Alternatively, the Na_xCoO_2 is considered to be located near the boundary between the antiferromagnetic metal and the correlated metal as in the case of the perovskite system $La_{1-x}Sr_xTiO_3$ with $x \approx 0.05$. It should be noted that many of the investigations performed to date are for the specimens annealed above T_{ac}. In order to clarify the properties of the present system completely, it is very necessary to know the absolute chemical composition of $Na_{x-\delta}Co_{1-\delta'}O_2$.

The first-order phase transitions of the electrical resistivities are observed irrespective of the cooling condition, which may be due to the ordering of Na ions. Since the susceptibility data do not exhibit any transition at the corresponding temperature, the resistivity anomaly is purely related to the charge dynamics. In addition, the irreversible transitions in the heated process are detected with the fast cooling (FC) down to a certain temperature. Our recent study for the single-crystal specimens with $0.48 \leq x \leq 0.65$, outside of the composition for the present specimens, does not exhibit these transitions at temperatures below room temperature [2]. The difference for the resistivity anomalies may be due to the metastability in the local structure of the polycrystalline specimens rather than the difference of the composition, which should be revealed from a microscopic point of view.

As shown in Fig. 1, the NMR spectrum of ^{23}Na nuclei in $Na_{0.8}CoO_2$ consists of two kinds of peaks, expected from a presence of two independent Na sites in the crystal structure. The hyperfine field trans-

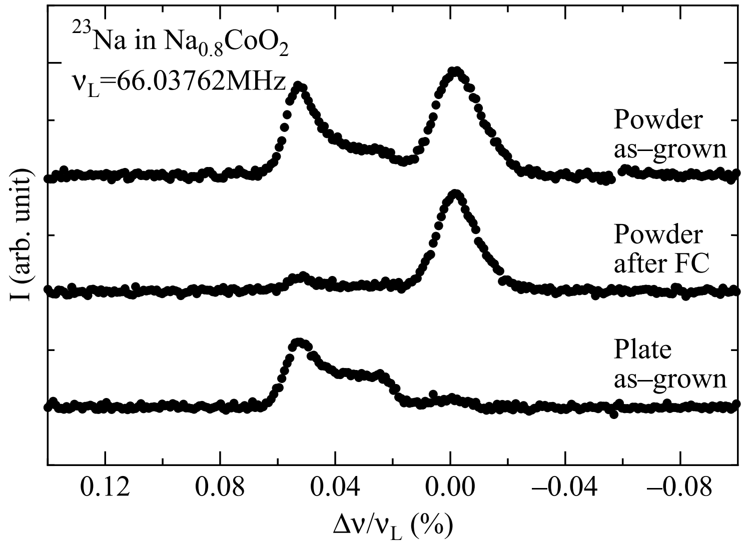

Fig. 1. The NMR spectra of ^{23}Na nuclei in $Na_{0.8}CoO_2$ at room temperature.

ferred from Co ions for the Na1 site is considered to be larger than that for the Na2 site. Thus, the spectrum with a large shift may come from the Na1 site. After FC, the signal changes clearly as compared with that for the as-grown specimens. This suggests the rearrangement of Na1 ions, which is likely related to the irreversible transition of the resistivity described above. In addition, the *Q*-factor of NMR coil after FC increases as compared with that for the as-grown specimen, suggesting that the FC process leads to an increase of the resistivity. It is quite likely that the irreversible transition of resistivity comes from the metastability in the local structure of polycrystalline sample, since it is known that a fast cooling induces a metal−semimetal transition in the organic superconductor.

The ^{59}Co-NMR study in the triangular lattice superconductor $Na_{0.3}CoO_2 \cdot 1.3H_2O$ is also being performed, which will be reported in future.

The NMR measurements described here have been done in collaboration with Y. Uchida, National Institute for Materials Science.

References

[1] T. Ikeda and M. Onoda: J. Phys.: Condens. Matter **18** (2006) 8673–8682.

[2] M. Onoda and T. Ikeda: J. Phys.: Condens. Matter **19** (2007) 186213 (14pp).

3.5 Estimation of Eu concentration in Eu-doped GaN by RBS measurements

J. Sawahata, J.W. Seo, S.Nemoto and K. Akimoto

Rare earth (RE) doped GaN thin films have attracted great interests due to their unique optical properties, that is, luminescence due to an intra 4f transition of RE ion depends very little on the host material and the temperature. Among the several RE dopants, it is well known that europium (Eu) shows a strong red emission around 622 nm. The Eu concentration in the films is a one of important parameters on the optical properties of Eu-doped GaN. Therefore, we performed Rutherford back scattering (RBS) measurements to estimate Eu concentration in Eu-doped GaN.

The Eu-doped GaN thin films were grown on GaN/Al_2O_3 substrates by molecular beam epitaxy methods [1]. The RBS measurements were carried out using 1.5 MeV accelerated ^{4}He ions with a tandem accelerator placed at UTTAC. The geometry of incident angle, exit angle and scattering angle were 30, 0 and 150 degrees, respectively. A detector was placed at 70 mm from the sample surface.

Fig. 1 shows a RBS spectrum of Eu-doped GaN as an example. The spectrum heights of the edges corresponding to scattering from the surface atoms were used for calculation of Eu concentration. In Fig.1, the Eu concentration was estimated at 3 at.%. The red emission intensity of Eu-doped GaN increased up to an Eu concentration of 3 at.%, and then it decreased for Eu concentration of more than 3 at.%. Therefore, we found that an optimum Eu concentration on the optical properties of Eu-doped GaN is estimated around 3 at.% by RBS measurements.

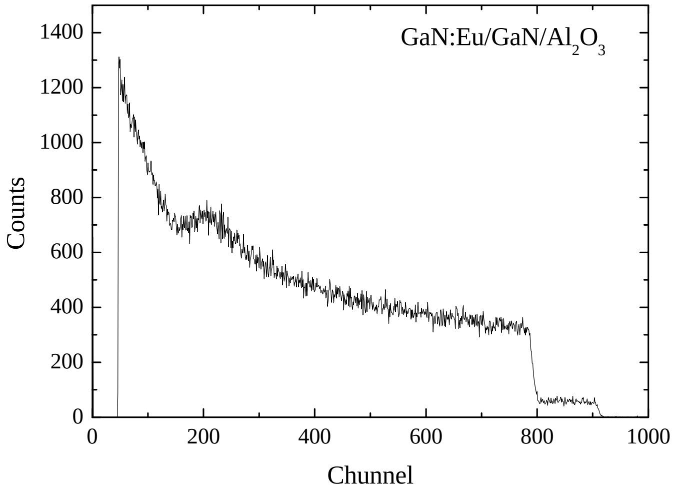

Fig. 1 RBS spectrum of Eu-doped GaN

References

[1] H. Bang, S. Morishima, J. Sawahata, J. Seo, M. Takiguchi, M. Tsunemi, K. Akimoto, Appl. Phys. Lett. 85, 227 (2004)

3.6 Conversion Electron Möessbauer Spectroscopy (CEMS) of γ-Fe_2O_3 epitaxial thin films

M. Minagawa, Y. Toyoda, M. Hasegawa, H.Yanagihara and Eiji Kita

Recently, growth techniques for γ-Fe_2O_3 epitaxial films have been developed by several groups[1, 2]. An detailed x-ray diffraction analysis revealed that the unit cell of the grown film is three times larger than that of Fe_3O_4[2] and that the B-site vacancies are fully ordered along *c*-axis parallel to the film growth direction. The thickness of the film was around 10 nm and its CEMS was examined last year.[3] From the preliminary experiment, it is found that physical properties were getting similar to those of Fe_3O_4 when the film thickness was increased more than 20nm. This fact implies that the electronic structure and vacancies on spinel B sites are dependent on the film thickness.

Use of ^{57}Fe enriched materials has been a powerful tool for the Mössbauer spectroscopy because natural abundance of Mössbauer active ^{57}Fe atoms is only 3 % and rest of Fe atoms, ^{56}Fe, are not Mössbauer nuclei. Especially for thin film researches, the enrichment with ^{57}Fe is has been used to pronounce magnetic properties at the limited area such as surface and interface regions.

In this report, dependence of the structure on the thickness of γ-Fe_2O_3 epitaxial films grown on MgO(001) was examined by inserting ^{57}Fe oxide layers during the deposition. The film growth method was the same as the way reported in the last annual report. We performed conversion electron Mössbauer spectroscopy (CEMS) at room temperature.

Single crystal thin films were prepared with a reactive vacuum deposition technique on MgO(001) single crystal substrates.[2] Ozone of 10^{-6} Torr was used as a reactive gas during deposition. The samples to survey the thickness variation of the structure was made by placing 5nm of ^{57}Fe oxide layers always 5 nm apart from the top of the film surface. The outermost 5 nm was made of natural Fe(not enriched) to avoid the influence from the surface. 4 samples with different total thickness were prepared and schematically illustrated in Fig. 1. It is noted that the thickness used here is a nominal thickness of metallic iron then actual thickness of the oxide will be about 1.3 times thicker.

CEMS spectra with different locations of the ^{57}Fe enriched layer are shown in Fig. 2. The spectrum for the 10 nm sample mainly consists of a subspectrum originated from Fe^{3+} ion. Small amount of a subspectrum with smaller hyperfine field was observed in the 20 nm sample. This subspectrum became clear when the total thickness increased. For the sample(d), the area ratio of the subspectra to the Fe^{3+} subspectrum was roughly estimated to be 0.5 and its hyperfine parameters were agreed with those of $Fe^{2.5+}$

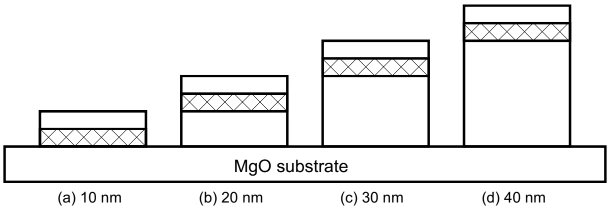

Fig. 1. Samples for the thickness dependent Conversion Electron Mössbauer Spectrum(CEMS) of γ-Fe_2O_3 films. The hatched area depicts the location of 5 nm ^{57}Fe layers for each sample.

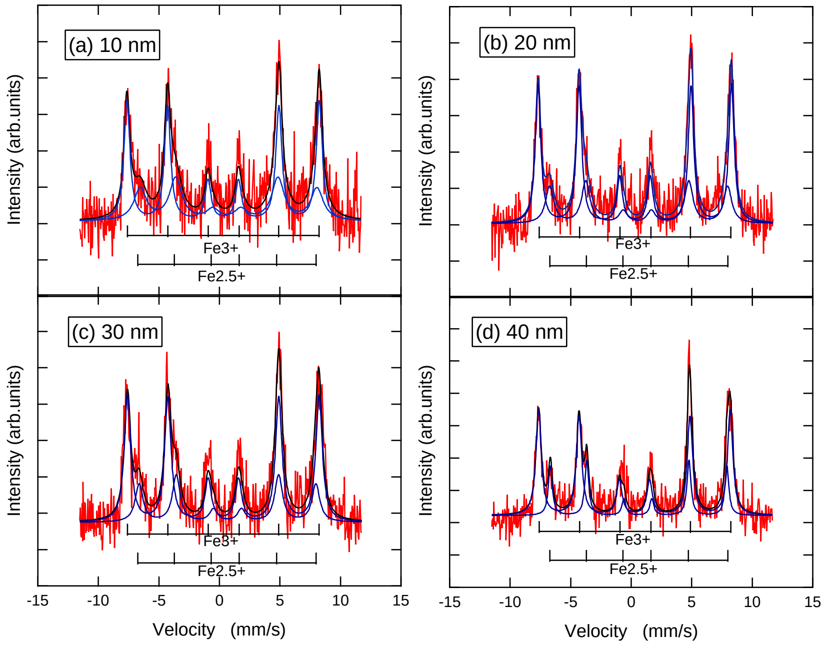

Fig. 2. Conversion Electron Mössbauer Spectra(CEMS) of γ-Fe_2O_3 films with the different location of ^{57}Fe layers, which is schematically described in Fig. 1.

ions observed in Fe_3O_4. The $Fe^{2.5+}$ subspectrum observed in stoichiometric Fe_3O_4 has an area ratio of 2 against the Fe^{3+} subspectrum. Therefore, the Fe oxide thin film prepared with the present technique is composed of γ-Fe_2O_3 when the thickness is less than 20 nm and tends to be a intermediate phase between γ-Fe_2O_3 and Fe_3O_4. It is supported by the increase of $Fe^{2.5+}$ subspectrum area in the CEMS spectra.

RHEED observation revealed that the crystal structure dose not change during deposition. This fact implies that the basic crystal structure keeps spinal-type when the thickness increases. To keep γ-Fe_2O_3 phase stable in more thicker films, it might be necessary to precisely control a condition of Ozone gas sources. Signal to noise ratios were remarkably dropped compared with the γ-Fe_2O_3 thin film with 7 nm in thickness(5 nm in nominal Fe thickness). Improvement of the S/N ratio in the CEMS study will lead to clear conclusion in this study.

References

[1] F. C. Voogt, T. Fujii, P. J. M. Smulders, L. Niesen, M. A. James and T. Hibma, Phys. Rev. B **60** (1999) 11193.

[2] H. Yanagihara, M. Hasegawa, E. Kita, Y. Wakabayashi, H. Sawa, and K. Siratori, J. Phys. Soc. Jpn. **75** (2006) 054708.

[3] M. Hasegawa, K. Shibata, H. Yanagihara, E. Kita, *UTTAC Annual report 2005* (University of Tsukuba, 2006) p.29, M. Hasegawa, H. Yanagihara, Yuta Toyoda, Eiji Kita, L. Ranno, J. Magn. Magn. Mater. **310** (2007) 2283.

4.

ION BEAM ANALYSIS AND APPLICATION

4.1 Status of Tsukuba AMS system

Y.Nagashima, K.Sasa, T.Takahashi, Y.Tosaki, M.Tamari, B.Zhou, K.Sueki, K.Bessho, H.Matsumura, T.Miura and K.Masumoto

In parallel with the AMS measurements, the improvements of both an AMS ion source system and terminal stabilization system have been done. First, the improvements done this year, and second, the experimental results are reported briefly.

The beam optics for the ion source has been improved and consequently the $^{35}Cl^-$ ion current increased from ~10μA to ~40μA. The strong $^{35}Cl^-$ current helps very much to realize the measurement of the samples with very small ^{36}Cl to ^{35}Cl ratio. The best configuration of the ion source we got is shown in Fig. 1. According to the result of the electric field calculation, the target voltage and the ionizer voltage are adjusted to -18kV and -16.5kV, respectively. Therefore, the sputtering energy of the Cs^+ beam is decreased from 2.5keV to 1.5keV. This low energy of the Cs^+ beam helps very much to measure the very small amount of sample such as less than 1mg of sample because of very small sample consumption. We understand that the shape of both an ionizer and an extraction electrode are not ideal. Therefore, they were replaced with newly designed one. The Cs^+ beam with about 2mm in diameter hits on the sample with 0.5mm radius and consequently the $^{35}Cl^-$ beam with about 2mm in diameter can be produced.

The stable operation of a terminal high voltage is essentially requested for the stable AMS measurement. A terminal voltage stabilizer uses the beam currents sensed by an image slit and keeps the terminal voltage stably. The accuracy of the terminal voltage, however, was insufficient for the accurate AMS measurements because of lack of the current sensitivity of the image slit. Therefore, in order to ensure the stable and accurate AMS measurements, an operation mode of the image slit has been changed from a continuous (DC) mode to a pulse operation mode. The pulse operation mode tremendously improves the sensitivity of the image slit and a fluctuation of the beam energy becomes smaller. As a result of this modification, the reproducibility of the ^{36}Cl to ^{35}Cl ratio of the standard sample by the AMS measurement has been improved from 10% to 2%.

The dating of ice core sampled at the Fuji dome in the Antarctica Continent as a big national project is in progress. The depth of the ice bed at the Fuji dome is about 3,000m and the core samples are collected from the surface to the 3,000m depth. It is estimated that the age of the core sample at the 3,000m depth is ~100 million years old. Therefore, it is expected that the core sample memorizes the record of not only an environmental change of the earth but also a change of a solar activities for the 100 million years. To investigate and to understand the change, our efforts have been bended on the measurements of ^{36}Cl element in the ice core by mean of ^{36}Cl-AMS.

A calculated fall out of the ^{36}Cl on the ice bed is ~60 atoms/m^2/s and the number of the ^{36}Cl in the ice core is ~6×10^3 atoms/g. The $^{36}Cl/Cl$ ratio is estimated to be the range from 10^{-14} to 10^{-15}. To accommodate lowering the $^{36}Cl/Cl$ ratio, several improvements have been performed both on the AMS ion source.

The distance between ^{127}I- ion trajectory and ^{129}I- one is only ~3mm at an image point of the 120 degree magnet. The ~3mm separation is insufficient to measure both ^{127}I- and ^{129}I- correctly because the both particles are overlapped and a part of ^{129}I- particles are intersected by a Faraday cup with which the ^{127}I- current is measured. This missing of ^{129}I measurement caused a lowering of efficiency and accuracy of the ^{129}I AMS measurement. Therefore, in order to improve the accuracy of ^{129}I to ^{127}I ratio measurement, a new ^{127}I beam deflector is installed in a 120 degree scattering chamber. The distance between ^{127}I$^-$ ion trajectory and ^{129}I$^-$ one is expanded from ~3mm to ~9mm. The ~9mm distance is sufficient to be able to measure ^{127}I- without any disturbance on the ^{129}I$^-$ particle.

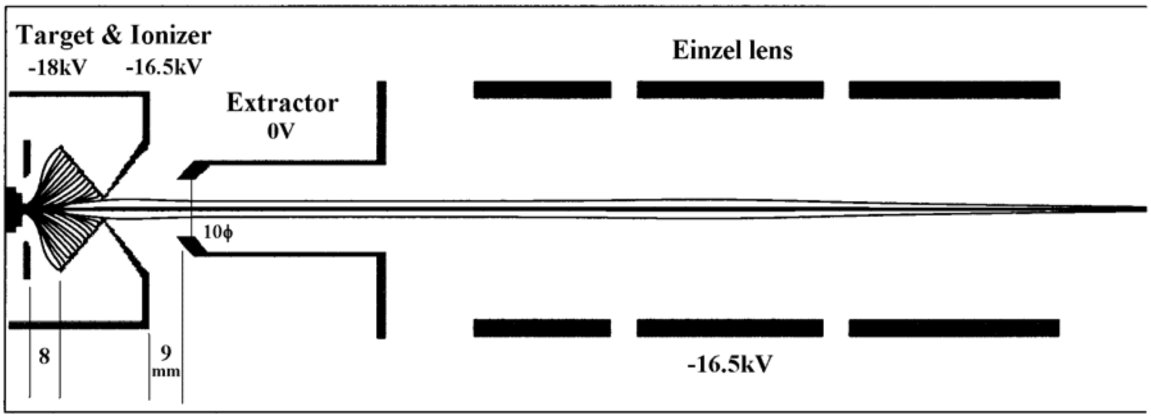

Fig. 1 Calculation of Cs$^+$ beam trajectories and ^{36}Cl$^-$ beam envelope at the ion source and an einzel lens. The diameter of the Cs+ beam spot on the sample is about 2.0mm.

4.2 ^{129}I AMS by a ^{97}Mo^{16}O$_2$ molecular pilot beam method

B.Zhou, Y.Nagashima, K.Sasa, T.Takahashi, Y.Tosaki, M.Tamari, K.Sueki, K.Bessho, H.Matsumura, and T.Miura

A Tsukuba AMS system is now used for the steady measurements of ^{26}Al and ^{36}Cl in the various research fields such as the environmental sciences. Adding to these elements, ^{129}I high sensitive measurement by the mean of the AMS is strongly requested because the ^{129}I measurement with a thermal neutron activation method shows the limits. The sensitivity of the method is limited to about 10^{-8} order of the ratio of ^{129}I to ^{127}I. The ^{130}I-decay γ measurement are strongly disturbed by the ^{130}Xe-decay γ because both γ lays have almost the same energies, E=536KeV. And consequently, the sensitivity of ^{129}I measurement by the neutron activation method is limited to 10^{-8}. On the other hand, the ^{129}I-AMS has no isobaric disturbance and enables us to measure ^{129}I with very high sensitivity such as 10^{-13} ratio.

Fig. 1 shows the outline of the Tsukuba ^{129}I-AMS system. As we have already reported in somewhere [5-7], in stead of a generating voltage feedback method, a molecular pilot beam feedback method is introduced. An acceleration voltage of the tandem accelerator can be kept within 0.1% accuracy with the pilot beam method. Maximum voltage of the tandem is up to 12MV and this high voltage makes us easier to identify ^{26}Al or ^{36}Cl elements from isobaric elements such as ^{26}Mg or ^{36}S. Two thin, 10μg/cm2, stripper foils are used. One is set in the terminal section as a charge exchange foil and second one is prepared in the AMS beam line in order to sweep out the pilot beam by following an energy and a momentum selector.

An electric beam deflector has been installed in a vacuum chamber located at an 120 degree dipole magnetic in the ion source section. Fig.2 shows the beam deflector. The purpose of this installation is to expand the separation between a 129I- ion trajectory and a 127I- ion one. We are expecting the 127I- current can be measured more precisely by using this deflector and consequently more accurate measurement might be realized.

In order to know the background level of the ^{129}I measurement, two kinds of samples are measured. These are a sample of only ^{97}MoO$_2$ molecular element, and a mixture of AgI reagent and ^{97}MoO$_2$. Fig. 3 shows the results of these measurements. The separation of ^{97}Mo and ^{129}I is perfect and ^{97}Mo causes no influence on the ^{129}I counting. In case of ^{97}MoO$_2$ solo sample, there is no observation in the region of ^{129}I collection. On the other hand, in the AgI reagent measurement, seven (7) ^{129}I counts are detected. These elements apparently came from AgI reagent itself, not from the system, because of no ^{129}I detection in the measurement of ^{97}MoO$_2$ sample. If we consider one event in the seven is originated from the system background, the one count corresponds to $1\text{x}10^{-13}$ ratio of ^{129}I to ^{127}I. Though we are confident that the system background is lower than $1\text{x}10^{-13}$, at this moment, we say that $1\text{x}10^{-13}$ is the maximum sensitivity.

Three samples are prepared by diluting the NIST high level ^{129}I standard, SRM-3231. The ratios of ^{129}I to ^{127}I of these standards are carefully estimated to be 7.0×10^{-10}, 6.9×10^{-11}, and 7.0×10^{-12}. In order to get suitable ^{97}Mo^{9+} current that is used to control the acceleration voltage of the tandem, the mixture ratio of the AgI sample to $^{97}Mo^{16}O_2$ element is controlled to be 10. The energy spectra of these samples are shown in the Fig. 4. Similar to the background measurements, the ^{129}I yields are clearly identified from the yield of ^{97}Mo. Therefore, instead of the TOF detector, a SSD detector is used for the measurements because of no appearance of disturbance by the background. Linearity and re-productivity of the measurements are checked with three samples. The ratios of ^{129}I to ^{127}I of the samples are reasonably large and spread from 10^{-11} to 10^{-9}. Though the numbers of measurements are only three, we can probably say that the accuracy of our ^{129}I-AMS measurement is within 3% in the range of 10^{-9} to 10^{-11} ratio of ^{129}I to ^{127}I. A flat top characteristic at the terminal stripper foil was measured and it was ~3 gauss. The 3 gauss flat top corresponds to 0.1 % stability. This 3 gauss is enough to keep the stable transmission of the ^{129}I particles because the stabilities of all of the electric equipment used in the tandem are better than 0.01%.

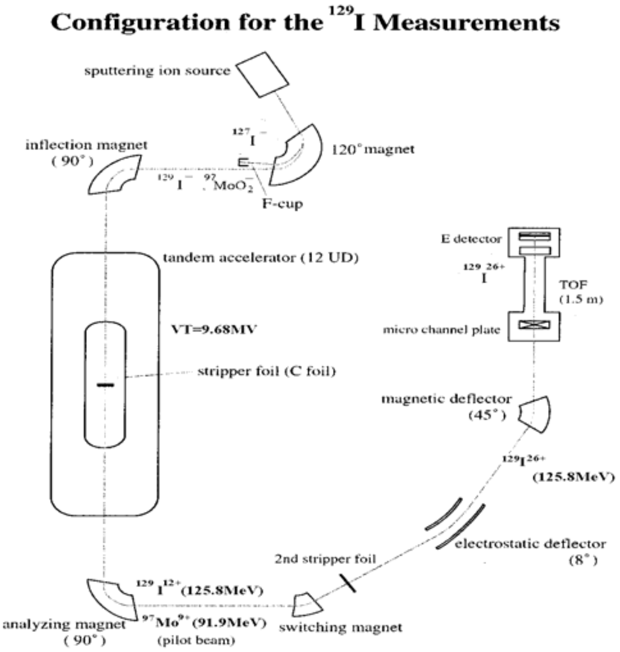

Fig.1 Outline of the Tsukuba ^{129}I AMS system

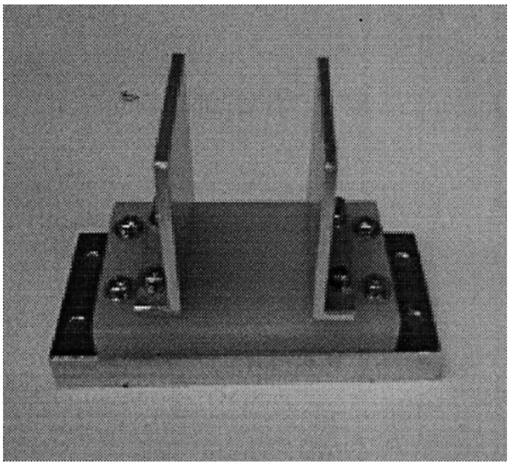

Fig. 2 An electrostatic deflector for ^{127}I

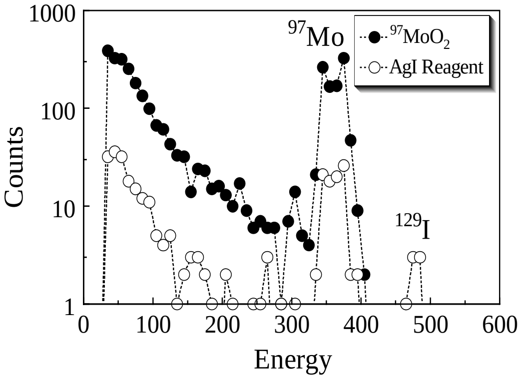

Fig. 3 Background measurements

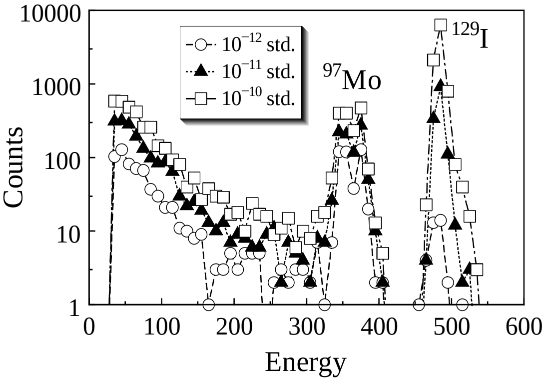

Fig. 4 Standard samples

4.3 ^{36}Cl concentrations in the Dome Fuji ice core, Antarctica.

K. Sasa, Y. Matsushi, Y. Tosaki, M. Tamari, Y. Nagashima, T. Takahashi, K. Sueki, K. Bessho[1], H. Matsumura[1], Y. Shibata[2], H. Motoyama[3] and K. Horiuchi[4]

The concentration of cosmogenic radioisotopes in the ice core provide useful information about the history of the cosmic ray flux in the atmosphere, the past solar activity and the past earth environment such as changes in the geomagnetic field. We have been taking part in the joint research project to investigate the variation of the cosmogenic radioisotopes ^{10}Be ($T_{1/2}$ = 1.51 × 10^6 years), ^{26}Al (7.16 × 10^5 years) and ^{36}Cl (3.01 × 10^5 years) in the ice core retrieved from the Dome Fuji station in collaboration with National Institute of Polar Research, National Institute for Environmental Studies, Hirosaki University and the University of Tokyo. We present here the first results of the cosmogenic radioisotope ^{36}Cl measurements in the deep ice core samples at the Dome Fuji station (DF02). ^{36}Cl–AMS was performed with the energy of 100 MeV by using a multi-nuclide AMS system at the University of Tsukuba (Tsukuba AMS system) [1]. In this study, we used the 1.5 m long cut sample of the DF02 core in the range from 2400 to 3028 m. The typical weight of the 1.5 m long cut sample was approximately 140 g. We merged 5 to 8 samples together for ^{36}Cl-AMS measurements. After adding 0.75 mg of stable chlorine as carrier to the integrated sample, ^{36}Cl and the carrier were extracted together by means of anion exchange resin. The sample was prepared as AgCl, and a saturated benzene solution of fullerene (C_{60}) was added to it for the $^{12}C_3^-$ pilot beam method [1].

In the year of 2006, we measured 13 samples in the DF02 core to estimate the ice core age by the ^{36}Cl radioactive decay. The measured ^{36}Cl/Cl ratios were in the range of 5.4 – 29.1 × 10^{-14}. The ^{36}Cl concentrations in the DF02 core correspond to 0.14 – 0.60 × 10^4 atoms g^{-1}. There are some relationships comparison between the ^{36}Cl concentrations and the paleoclimatic parameter δ^{18}O. The ^{36}Cl fluxes range with 0.42 – 2.18 × 10^4 atoms cm^{-2} yr^{-1}, which are calculated by the accumulation rate [2] estimated from δ^{18}O data. The ^{36}Cl fluxes in the deep ice core are decreasing with the depth. This result agrees with the radioactive decay of ^{36}Cl. Once locked in the ice, only the radioactive decay is responsible for a reduction of the cosmogenic radioisotope with age. This suggests that the ^{36}Cl analysis will be able to provide age constraints for the deep ice core.

Acknowledgements

This work is supported in part by the Grants-in-Aid for Scientific Research Program of the Ministry of Education, Culture, Sports, Science and Technology, Japan.

References

[1] K. Sasa et al., Nuclear Instruments and Methods in Physics Research B 259 (2007) 41–46.

[2] K. Satow et al., Polar Meteorol. Glaciol., 13 (1999) 43-52.

---

[1] Radiation Science Center, High Energy Accelerator Research Organization

[2] National Institute for Environmental Studies

[3] National Institute of Polar Research

[4] Hirosaki University

4.4 Chlorine-36 in precipitation in Tsukuba

Y. Tosaki, N. Tase, K. Sasa, T. Takahashi, Y. Matsushi[1], M. Tamari, Y. Nagashima, K. Sueki, K. Bessho[2] and H. Matsumura[2]

The meteoric ^{36}Cl is mainly produced through the spallation reaction, ^{40}Ar(p,α)^{36}Cl, in the stratosphere. After about two years [1], stratospheric ^{36}Cl enters the troposphere and is washed out by precipitation within a mean residence time of one week [2]. This meteoric input of ^{36}Cl to groundwater, along with marine-derived stable chlorine, is reflected as the background ^{36}Cl/Cl ratio of groundwater. Knowledge of this ratio is important in order to apply cosmogenic or bomb-produced ^{36}Cl as tracers in groundwater hydrology.

For the purpose of determining the recent background ^{36}Cl/Cl ratio in Tsukuba, bulk precipitation samples were collected from April 2004 at the roof of the Natural Sciences building, University of Tsukuba. The precipitation sampler used in this study consists of a PE funnel (diameter 15 or 21 cm), a HDPE bottle (3 or 5 L) and a specially developed glassware with a ping-pong ball, which prevents evaporative loss of the sample [3]. After being passed through a 0.45 μm filter, samples were processed by employing anion-exchange column method [4] and the ^{36}Cl/Cl ratios were measured by the Tsukuba AMS system.

The results of ^{36}Cl measurement for monthly precipitation samples (from April 2004 to May 2006, except for December 2005) are given in Fig. 1. A clear seasonal variation with peaks in the spring (April or May) was observed in ^{36}Cl concentration and flux. Similar spring maximum was reported in other locations [5,6] and for other cosmogenic radionuclides (e.g. ^{7}Be [7]). As pointed out in these studies, the seasonal pattern may be attributed to annual variation of tropopause height [8]. According to ref. [8], the tropopause begins to rise rapidly in April or May at mid-latitudes (especially about 30–40°N). As the tropopause rises, stratospherically produced ^{36}Cl is transported into the troposphere and washed out from the atmosphere after about one week. This mechanism would explain our observation.

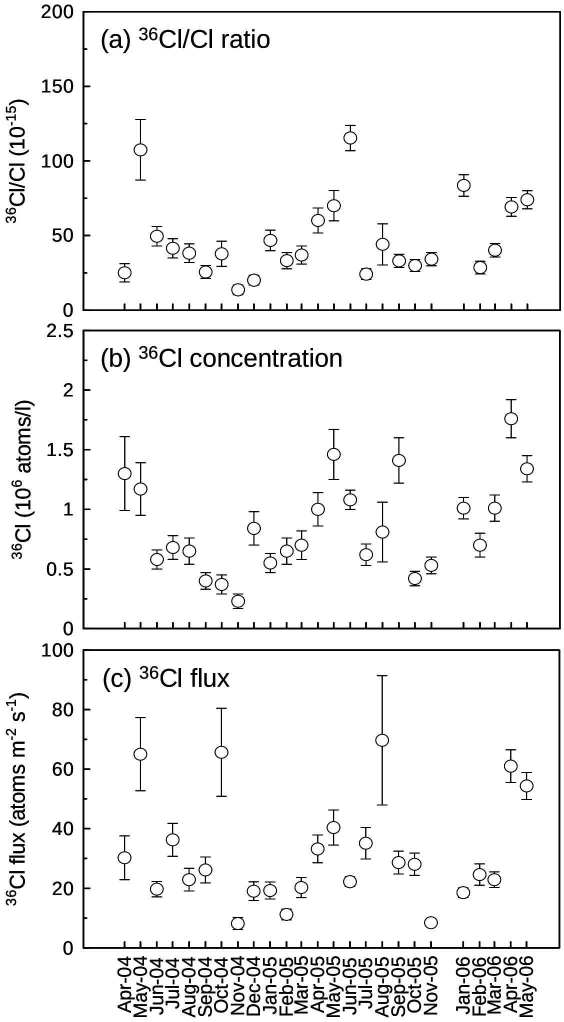

Fig. 1. ^{36}Cl in bulk precipitation samples.

---

[1] Present address: Department of Nuclear Engineering and Management, School of Engineering, The University of Tokyo

[2] Radiation Science Center, High Energy Accelerator Research Organization (KEK)

The measured ^{36}Cl/Cl ratios range from (1.4 ± 0.3) × 10^{-14} to (1.15 ± 0.08) × 10^{-13}. The average ^{36}Cl/Cl ratio for the entire sampling period is (3.9 ± 0.2) × 10^{-14}. This ratio would be interpreted as the recent background level in Tsukuba, whereas it disagrees with the ^{36}Cl/Cl ratio of a shallow groundwater sample, (1.19 ± 0.48) × 10^{-13}, obtained from an observation well (depth of about 2 m from the surface) at Terrestrial Environment Research Center, University of Tsukuba in 2003. This may suggest another source of ^{36}Cl after the deposition of meteoric ^{36}Cl. However, the contribution of epigene ^{36}Cl (^{36}Cl produced in surface rocks or soils) to groundwater is generally small compared to meteoric input [9].

Further investigation is needed to explain this disagreement. We are planning to measure some water samples with minimum anthropogenic effects such as springs or stream waters around Mt. Tsukuba.

Acknowledgements

We thank Dr. Shiho Yabusaki (Department of Environment Systems, Faculty of Geo-Environmental Science, Rissho University) for her advice on precipitation sampling.

References

[1] H.-A. Synal, J. Beer, G. Bonani, M. Suter, W. Wölfli, Nucl. Instr. and Meth. B 52 (1990) 483.

[2] H.W. Bentley, F.M. Phillips, S.N. Davis, in: P. Fritz, J.-Ch. Fontes (Eds.), Handbook of Environmental Isotope Geochemistry, Vol. 2, Elsevier, Amsterdam, 1986, p. 427.

[3] J. Shimada, J. Matsutani, S. Dapaah-Siakwan, M. Yoshihara, K. Miyaoka, A. Higuchi, Ann. Rep. Inst. Geosci. Univ. Tsukuba 20 (1994) 11.

[4] Y. Tosaki, R. Seki, UTTAC Annual Report 2005 (2006) 40.

[5] D.L. Knies, D. Elmore, P. Sharma, S. Vogt, R. Li, M.E. Lipschutz, G. Petty, J. Farrell, M.C. Monaghan, S. Fritz, E. Agee, Nucl. Instr. and Meth. B 92 (1994) 340.

[6] L.J. Hainsworth, A.C. Mignerey, G.R. Helz, P. Sharma, P.W. Kubik, Nucl. Instr. and Meth. B 92 (1994) 345.

[7] J.E. Dibb, J. Geophys. Res. 94 (1989) 2261.

[8] D.O. Staley, J Atmos. Sci. 19 (1962) 450.

[9] F.M. Phillips, in: P.G. Cook, A.L. Herczeg (Eds.), Environmental Tracers in Subsurface Hydrology, Kluwer, Boston, 2000, p. 299.

4.5 Estimation of thermal neutron fluences in the concrete of various accelerator facilities by ^{36}Cl AMS

K. Bessho[1], H. Matsumura[1], T. Miura[1], K. Masumoto[1], T. Suzuki[1], H. Hagura[1], Y. Nagashima, K. Sasa, T. Takahashi, R. Seki, K. Sueki, Y. Tosaki, Y. Matsushi, M. Tamari

At accelerator facilities, concrete components around beam lines are exposed to secondary particles during machine operation, and various radionuclides are accumulated in the concrete. Thermal neutron fluence generated during machine operation is useful information to estimate the radioactivities of the induced nuclides because most of the radionuclides are mainly produced by thermal neutron-capture reactions. Our group has studied the behavior of neutrons inside concrete walls and floors at various accelerator facilities by ^{36}Cl-AMS, and the thermal neutron fluence inside the concrete had been discussed based on energies of secondary neutrons.[1,2]

In FY 2006, the concrete samples obtained at the Neutrino Beam Line (KEK) were measured. In order to clarify the origin of the thermal neutrons inside the concrete, distributions and energies of neutrons were calculated by the MARS code simulation. These results show that thermal neutrons observed at deeper positions were mainly generated by thermalization of fast-neutrons. Direct penetration of thermal neutrons from the concrete surfaces was found to be small contributions to thermal neutrons occurred inside the concrete. The analysis of concrete-cores sampled at different positions in the Neutrino Beam Line will be continued in FY 2007.

The concrete samples obtained at the buildings of UTTAC Pelletron 12UD were also analyzed in this year. Concrete was sampled just under the analyzing magnet, the surface of the floor, and the ^{36}Cl/^{35}Cl ratio in the concrete was analyzed by ^{36}Cl-AMS. The ^{36}Cl/^{35}Cl ratio at the floor surface was determined to be $(2.66\pm0.12) \times 10^{-12}$, and the thermal neutron fluence was estimated to be $(6.09\pm0.27) \times 10^{10}$ n/cm^2. This value is two to four orders smaller than other accelerators, such as SF-cyclotrons, 1.3GeV electron synchrotron, and 300MeV electron LINAC.[3] It demonstrated that ^{36}Cl-AMS is highly sensitive and useful for estimating thermal neutron fluences inside concrete samples, because the gamma-emitting nuclides, such as ^{60}Co and ^{152}Eu, could not be detected by gamma-ray spectrometry for the same concrete sample.

References

[1] K. Bessho *et al.*, *Radiochim. Acta,* **94**, 801 (2006)
[2] K. Bessho *et al.*, *Nucl. Instr. Meth. B* in press
[3] K. Bessho *et al.*, *UTTAC Ann. Rep. 2006,* 42

---

[1] High Energy Accelerator Research Organization

4.6 Chemical compositions and ^{36}Cl contents in chondritic meteorites

Y. Oura[1], S. Yamazaki[1], M. Ebihara[1],Y. Tosaki, K. Sasa, Y. Nagashima, T. Takahashi, Y. Tosaki,
Y. Matsushi, M. Tamari, K. Sueki, H. Matsumura[2], K. Bessho[2], T. Miura[2]

Meteorites contain stable and radioactive cosmogenic nuclides, which are produced by nuclear reactions with high energy cosmic rays during their flights in the space. Cosmogenic nuclides in meteorites provide important cosmochemical information of the meteorites, e.g. some kinds of age, a size before falling on the earth, and so on. ^{36}Cl is a one of the cosmogenic nuclides and produced by several nuclear reactions such as proton and neutron induced spallation reactions (main target elements: K, Ca, Ti, Cr, Mn, Fe, and Ni) and neutron capture reaction (target nuclide: ^{35}Cl). ^{36}Cl in the metal phase mostly consisting of Fe-Ni alloy in Antarctic meteorites was used to determine their terrestrial age [1, 2] . On the contrary, it is not easy to use ^{36}Cl in silicate phase to get meaningful cosmochemical information because production sources of ^{36}Cl are complicated. However, since ^{36}Cl production excitation functions for proton induced spallation reaction are varied for different target elements, if production rates of ^{36}Cl for individual target elements are obtained, detailed irradiation condition must be estimated. In this study, as the first step for estimating the irradiation condition of chondrites using ^{36}Cl, we determined ^{36}Cl contents and chemical compositions for several phases separated from chondrites.

Two chondrites, Barwell and Allegan, were used in this sturdy. From powdered whole-rock samples, 6 phases with different elemental compositions were separated by both physical and chemical treatments. Chemical compositions of mainly target elements for bulk and 6 separated phases samples for each chondrite were determined nondestructively by neutron induced prompt gamma-ray activation analysis and instrumental neutron activation analysis. For AMS, AgCl precipitates were prepared for each powder samples. ^{36}Cl/Cl ratios were determined by AMS at the Tandem Accelerator Complex, University of Tsukuba.

In Table 1, chemical compositions and ^{36}Cl concentrations in the bulk and 6 phases for the Barwell meteorite are listed. The metal phase has the highest ^{36}Cl concentration (22.4 dpm/kg) and silicate phases contain similar ^{36}Cl contents (6.83 – 8.67 dpm/kg). A similar feature appears in the Allegan meteorites (24.7 dpm/kg for metal and 7.7 – 8.3 dpm/kg for silicatges). Calculation of ^{36}Cl production rate for each target element using simultaneous equations with chemical compositions and ^{36}Cl concentrations failed to yield reasonable values. Then, production rates for 2 elemental pairs, (K + Ca) and (Fe + Ni), which largely contribute to ^{36}Cl production, were calculated. Based on values in Table 1, chemical concentrations were recalculated assuming that a meteorite consists of 9 target elements only. ^{36}Cl concentrations are plotted against (K + Ca) or (Fe + Ni) concentrations, as shown in Fig.1. ^{36}Cl concentration is found to increase almost linearly with increasing of (K + Ca) concentration and to decrease with decreasing of (Fe + Ni) concentration. From the intercept with x = 100, values of 247 and 25 dpm/kg were obtained as approximate production rates for (K + Ca) and (Fe + Ni), respectively. Interestingly, similar values, 234

---

[1] Graduate School of Science and Engineering, Tokyo Metropolitan University
[2] Radiation Science Center, High Energy Accelerator Research Organization

and 24 dpm/kg, were obtained for the Allegan meteorite. Determination of Cl concentrations by radiochemical photon activation analysis is now in progress to estimate the contribution of ^{35}Cl (n, γ) reaction.

Table 1. Chemical composition and ^{36}Cl concentration in the Barwel meteorites.

	bulk	metal	silicate-1	silicate-2	silicate-3	silicate-4	silicate-5
K [%]	0.0839		0.0944	0.192	0.00517	0.120	0.00257
Ca [%]	1.33	0.0140	1.54	2.11	0.342	1.90	
Ti [%]	0.0693	0.00320	0.0618	0.149	0.0455	0.103	
Cr [%]	0.317	0.0138	0.362	0.661	0.0108	0.562	0.0178
Mn [%]	0.277	0.00585	0.280	0.243	0.165	0.211	
Fe [%]	23.7	82.4	18.7	7.82	30.5	6.75	28.9
Ni [%]	1.73	5.63	0.26		2.12		0.42
V [ppm]	67.8	1.2	4.6	132	2.6	114	
Co [ppm]	526	6690	110	4.99	1070	5.62	234
^{36}Cl [dpm/kg]	8.10	22.4	7.56	8.10	8.67	6.83	8.60

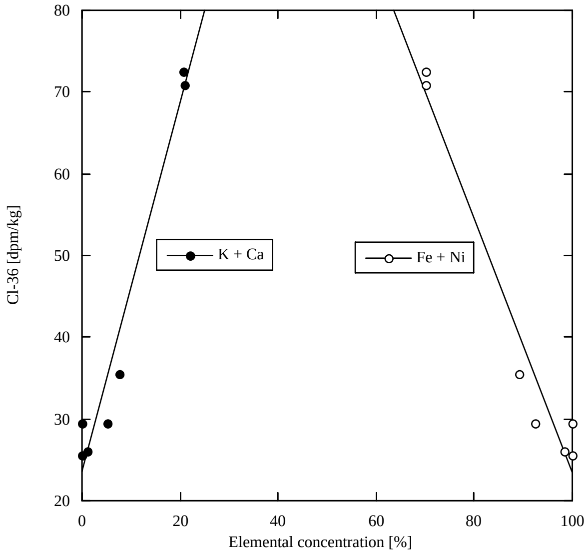

Fig.1. ^{36}Cl concentration vs. target elemental concentration for the Barwell meteorite.

References

[1] K. Nishiizumi, D. Elmore, P. W. Kubik, Earth Planet. Sci. Lett. 93 (1989) 299.

[2] K.C. Welten, K. Nishiizumi, M. W. Caffee, Lunar Planet. Sci. 31 (2000) #2077.

4.7 Quantitative PIXE analyses of fluid inclusions in quartz by using 1.92 MeV proton beam

M. Kurosawa, S. Ishii and K. Sasa

Fluid inclusions are important as the most convincing information of fluid activities and vein-type ore formation in the Earth. In particular, elemental compositions of fluid inclusions provide a direct evidence for chemistry of fluids and elemental transportation related to magmatic process. Thus, considerable efforts have been invested in the development of techniques for the precise quantitative elemental analyses using PIXE [1-4], SR-XRF [5,6], and LA-ICP-MS [7,8]. In this report, we describe micro-PIXE analyses of single fluid inclusions in quartz by using 1.92 MeV proton beam.

Samples used were fluid inclusions in a quartz crystal of hydrothermal vein from a Miocene Kofu biotite-granite, Yamanashi Prefecture, Japan. The quartz was cut and double-polished, and a halite-bearing polyphase inclusion (~30 wt.% NaCl eq.) in the quartz were measured. The fluid inclusion is an ellipsoidal shape, 58 x 58 x 96 μm in size, and the inclusion depth is 10 μm. The PIXE analyses were performed at the 1MV Tandetron. A 1.0 to 5.0 nA beam of 1.92-MeV proton was focused to a 96 x 108 μm spot on the sample using slits and magnetic lenses. The beam incidence was normal to the sample surface, and the X-ray measurement take-off angle was 45˚[9]. The characteristic X-rays excited by the incident beam were collected by the Si(Li) X-ray-energy detector (Gresham Co.) with a nominal resolution of 152 eV at 5.9 keV, and the spectra were recorded by a multi-channel analyzer. A 55-μm-thick Mylar film was used to attenuate the intense X-rays from the predominant light elements and to prevent the entry into the detector of protons scattered from samples. The total charge was determined by integrating the target currents, and all samples were analyzed to the integrated charges of 0.5 to 5.0 μC. Analytical points were chosen based on optical viewing using a CCD camera mounted on the microscope [9].

Quantification was performed based on the model of Kurosawa et al. [4]. Intensities of X-rays generated from fluid inclusions are decreased by the attenuation of energy of the incident protons and the absorption of the X-rays by a quartz matrix and the fluid (Fig. 1). In this model, the decrease of total X-ray intensities from a whole fluid-inclusion are calculated by considering sizes and depth of fluid inclusion, the major element composition, the densities of the matrix and the fluid, their proton-stopping powers, the X-ray production cross sections, and the X-ray absorption coefficients. Finally, element concentrations are calculated based on X-ray intensities corrected for the decrease and the detector sensitivity determined for each element. A shape of the fluid inclusion is assumed as an ellipsoidal equal to the size of the measured fluid inclusion. The inclusion sizes and depths (Fig. 1) were

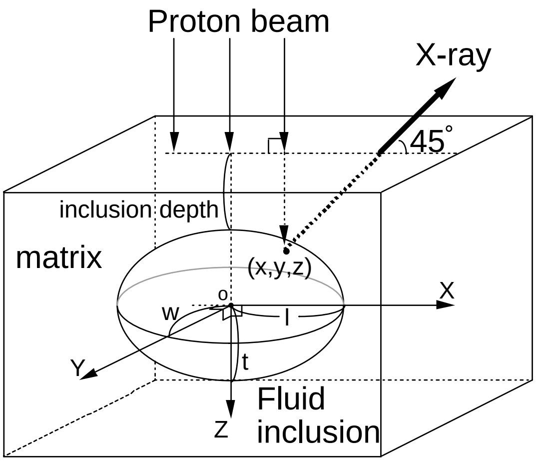

Fig.1. Schematic geometry for PIXE analysis of fluid inclusion

determined with an optical microscope. The inclusion depths are also exactly determined by measuring an intensity ratio of Cl K_{α} and Cl K_{β}. The fluid was approximated as 30wt.% NaCl solution. The detector sensitivity for each element was determined by measurements of thin-film multielement reference samples and a multi-element reference glass material NIST SRM 1412. The thin-film sample was prepared by dropping several standard solutions for ICP analysis onto a Mylar film and drying the film in a desiccator. In the calculations, contributions of X-rays from impurities in the matrix and bubbles in the fluid inclusion were corrected based on the method of Ryan et al. [1]. By using the calculation model, almost trace elements in fluid inclusions at levels of a few to several thousands ppm can be determined with the total analytical error of ±40 %[4]. Small halite, less than 20 μm in size, in fluid inclusions has no largely effect for the total analytical error.

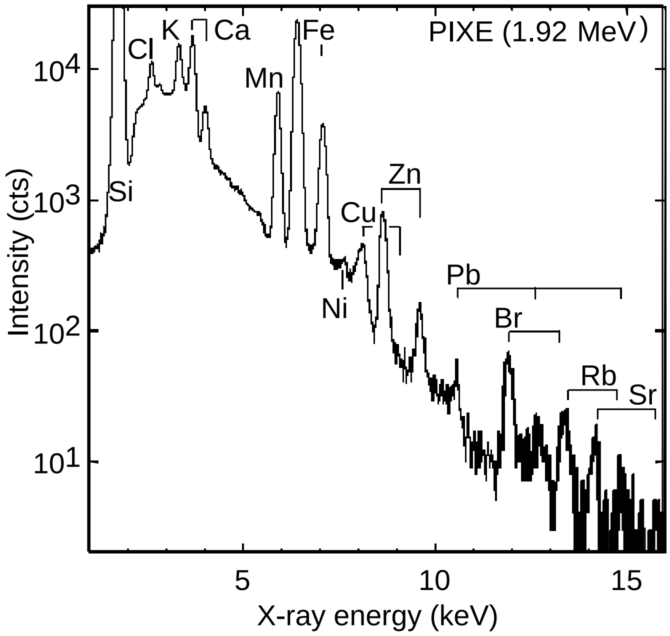

Fig.2. PIXE spectrum of halite-bearing fluid inclusion in hydrothermal quartz vein from the Kofu granite body

Observed spectrum of the fluid inclusion consisted mainly of the K-X ray peaks from Si, Cl, K, Ca, Mn, Fe, Cu, Zn, Br, Rb, Sr, and the L-X ray peaks from Pb (Fig. 2). The concentrations determined are as follows: 182000 wt. ppm for Cl, 20600 ppm for K, 14600 ppm for Ca and Fe, 3300 ppm for Mn, 1200 ppm for Zn, about 500 ppm for Cu and Br, and 120-180 ppm for Pb, Rb, and Sr. The values of almost transition metal elements were 2-3 times higher than those of two-phase fluid inclusions (~10 wt.% NaCl eq.) from miaroritic cavity in the granite. Thus, the enrichment could relate to a formation of hyper saline water and a metal separation by boiling of original low-saline fluids (~10 wt.% NaCl eq.) during adiabatic ascending from a deep part along the cooling joints of the granite body.

References

[1] C. G. Ryan et al., Nucl. Instr. and Meth. B77 (1993), 463.
[2] C. G. Ryan et al., Nucl. Instr. and Meth. B181 (2001), 570.
[3] V. S. Kamenetsky et al., Geology, 30 (2002), 459.
[4] M. Kurosawa et al., Geochim. Cosmochim. Acta, 67 (2003), 4337.
[5] P. Philippot et al. Chem. Geol., 144 (1998), 121.
[6] H. Nagaseki et al., Eur. J. Mineral., 18 (2006), 309.
[7] D. Günther et al., J. Anal. Atom. Spectrom., 13 (1998) 263.
[8] A. Audéat et al., Science, 279 (1998) 2091.
[9] M. Kurosawa et al., Nucl. Instr. and Meth. B142 (1998), 599.

4.8 First result of target preparation by the HIVIPP method in higher pressure than 1 atm.

I.Sugai[1], Y. Takeda[1], M. Oyaizu[1], H. Kawakami[1], K. Sasa, S.Ishii and K. Shima.

We recently developed a new deposition method of HIVIPP (HIgh energy VIbrational Powder Plating), which is based on the high energy vibrational motion of powder in the high electric field between parallel electrodes.

This method is very simple and does not require any complicated mechanisms. We have also found to be very useful as a target preparation technique in backed condition. The deposition process has been originally performed at room temperature and in vacuum. The deposition process could be further simplified if it could be carried out at higher than one atmospheric pressure with reactive gases or inert gases, without a vacuum pumping system. With this motivation, we have tried the target deposition of non-metallic silicon powders at high pressure of nitrogen, oxygen gases and air than one atm.. The first result is reported in this paper.

Fig. 1 shows a schematic view of the HIVIPP chamber for high pressure operation. The deposition container is identical with that mentioned in the previously papers [1–4], except for the high pressure container and the vacuum system. The deposition container is set in a high pressure container as shown in Fig. 1, which is composed of Acrylic tube pipe of 290 mm in diameter, 340 mm in high and 20 mm in the pipe thick.

We have investigated non-metallic Si powder for the first test deposition samples. As is well known, the element of Si have relatively high melting points of 1683 K. Both copper plates of 0.2 mm thick were used as a backing plate. The experimental apparatus is very simple, composed of two parallel metallic disks of 35 mm in diameter and 0.5 mm thick. These disks serve as the electrodes and hold the backing foil against the glass tube ring. We have also investigated the relationship between the deposition rates (μg/cm^2) versus high pressure. The deposition rate was tried at one atm. through 9 atm.. We used dried air as high-pressure gas. The powder to deposit was metallic Cr of nominal 60 μm in particle size and the deposition time was taken every 1 h. The thicknesses of the deposited targets were measured using an electronic ultra-microbalance. We used the copper foil of 0.2 mm thick as backing plate and measured the deposition rate in every one atm. from one atm. to 9 atm..

Fig. 2 shows the result obtained. Error bars represent the root mean square and the numbers attached to the points are the number of measured sample. From the picture, we can see the maximum deposition rate showed at the approximately 1.7 atm. of considerably low pressure and the rate was about 90 μg/cm^2/h on average. We can see also that after the 3 atm., the deposition rate was gradually decreased with the high pressure till 9 atm.. The deposition rate from 4 atm. to 9 atm. showed about 50 μg/cm^2/h on average. This rate is corresponding to nearly 1/2 of that 90 μg/cm^2 deposited at 1.7 atm.. The result shown in Fig. 2 gave us a vital role, because the HIVIPP method at only 2 atm. could be got the maximum deposition rate and

---

[1] *High Energy Accelerator Research Organization,Oho 1-1, Tsukuba, Ibaraki 305-0801, Japan*

this means that the handling for target deposition is very easy without any so danger due to low pressure. In addition to these, the high voltage to the electrodes could be applied 26 kV in maximum without the discharge. The voltage is very important parameter as mentioned in Ref.[1-3]. The deposition rate depends strongly on the voltage between the electrodes.

Next, in order to gain deeper insight into the observed color change of the Si deposited in the nitrogen, oxygen and air, we investigated the elemental Si deposited on copper backings of 0.2 mm thick. The light elements of C, N and O and other heavy elements of Si and Cu were detected by taking the PIXE using Si(Li) X-ray detector with a 1.92 MeV proton beams from the TANDETRON accelerator of University of Tsukuba.

The Si powder was obtained by agate mortal from Si wafer of high purity of 99.999 %. The target preparation of the Si was performed for 5 h at around 2 atm. Figure 3 shows the obtained spectrum. From the spectrum, we can see clear Si peaks. In the figure we can not see any clear nitrogen peaks in the nitrogen and air medium gases. On the other hand, we can see clear the oxygen peaks with rather strong from especially in the target prepared in only oxygen medium and also see oxygen peaks from other targets prepared in the air and nitrogen medium gases. The target prepared in vacuum of 5×10^{-4} Pa showed a small oxygen peak. Through these first detections, we have found that the nitrogen medium gas in filled HIVIPP chamber did not react with a high energy non-metallic Si powders and thus the color changed Si maybe be oxidized with the filled oxygen in the HIVIPP chamber.

As summary and conclusion, we have tried target depositions from the non-metallic Si powder by means of the HIVIPP method using high pressure medium gases over one atmosphere without vacuum pumping system.

The result showed the deposition rate did not depend strongly on the air pressure and the maximum deposition rate of 90 μg/cm^2/h on average around 1.7 atm..

We found that it did not detect any clear nitrogen peak in the deposited target in the nitrogen and air medium gases. On the other hand, the oxygen element in the Si targets by the both oxygen and the air medium gases were observed clear the strong oxygen peaks in the both targets. Further experiments are needed to confirm whether the nitrogen element in targets made in N_2 and air gases or not.

Reference

[1] I. Sugai, Nucl. Instr. and Meth. A397(1997) 81.
[2] I.Sugai, Nucl. Instr. and Meth.A438(1999)58.
[3] I.Sugai, Y.Takeda, H.Makii, K.Sano, Y.Nagai, Nucl. Instr.and Meth.A521(2004).
[4] I.Sugai, Y.Takeda, H.Kawakami, Nucl.Instr. and Meth.A561(2006)38.

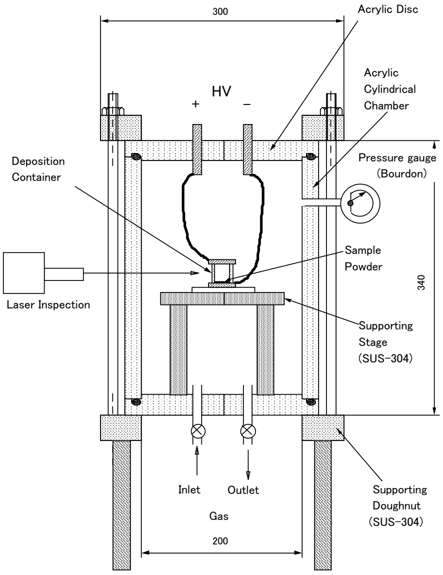

Fig.1 The HIVIPP chamber cross-sectional view for high pressure operation.

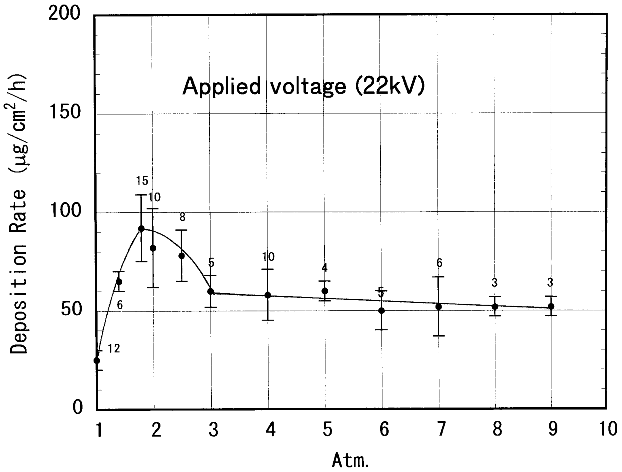

Fig.2 Deposition rate ($\mu g/cm^2/h$) as a function of applied high pressure of air (atm.).

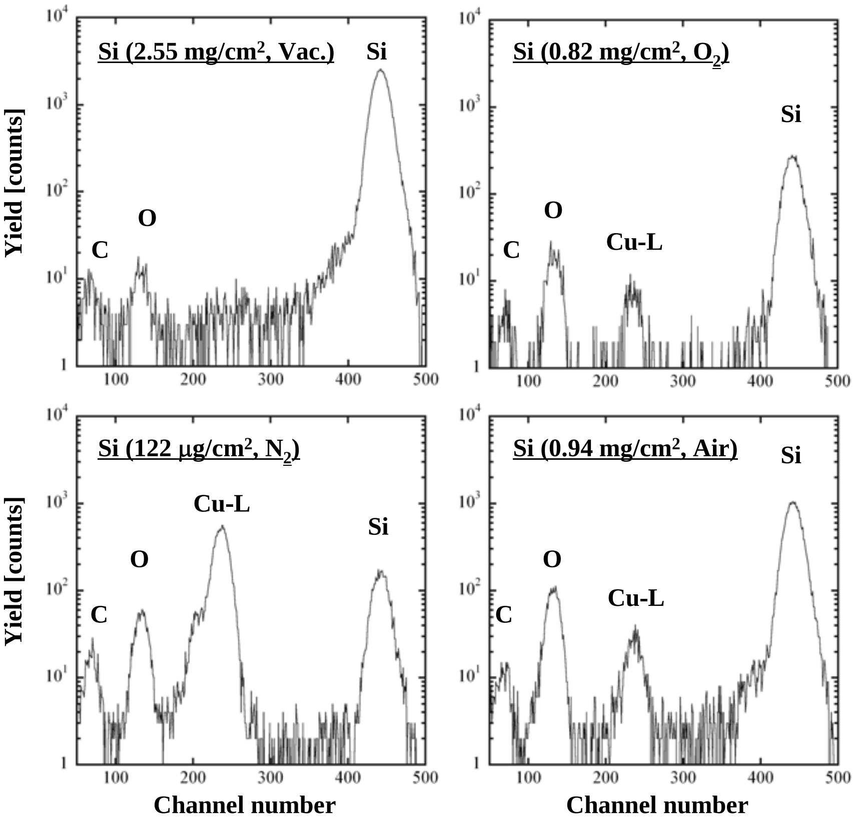

Fig.3 Elemental analysis of natural Si targets on copper backings made by the HIVIPP method in vacuum and 2.5 atm. pressure of air, nitrogen and oxygen. The spectra were obtained by the PIXE with a 1.92 MeV proton ion beams from the TANDETRON accelerator of University of Tsukuba.

4.9 High sensitive biosensors based on perforated waveguide structure

K. Awazu[1], M. Fujimaki[1], T. Komatsubara and Y. Ohki[2]

1. Introduction

We will report here on a strategy to perforate dielectric waveguides to enhance significantly the sensitivity of the sensor as firstly, the perturbation of the modes by adsorbed molecules is enlarged and secondly, their adhesion surface is increased. The holes in the insulator are created in the following way: the passage of an atomic particle through an insulator results in the creation of a cylindrical, latent nuclear track that extends along a straight line corresponding to the path of the atomic particle. The presence of tracks is revealed after etching in a suitable solution. However, the shape of the etched hole is often not cylindrical, but conical, with the largest diameter being near the surface. This is a consequence of the etching rate in the latent track being comparable to the general etching rate in the unirradiated region. Musket *et al.* have used vapor etching of ion tracks to create high aspect ratio, isolated cylindrical holes through ~600 nm-thick films of thermally grown silica on silicon [1]. In the present study, we have adopted the vapor etching technique to create cylindrical holes through silica waveguides.

2. Experimental

As glass substrate we used S-LAH66 glass (Ohara Co., Ltd.) with a high refractive index of 1.769. A 500nm thick-waveguide layer of a-SiO_2 film was deposited on an Au film on S-LAH substrate. Ion bombardment to perforate the waveguide was performed at room temperature at a residual pressure below 1×10^{-4} Pa. The 12 UD Pelletron tandem accelerator at University of Tsukuba was employed with 150 MeV Au^{14+} ions. To avoid overlap of the individual cylindrical holes, very low ion fluency was required. This was achieved by diffusing the ion beam through an aluminum foil in forward scattering geometry. 150 MeV Au^{14+} was reduced to 137 MeV Au^{30+} by passage through the Al foil. We performed vapor etching experiments with 20% hydrofluoric acid (HF). Influence of various liquid T_L and sample T_S temperatures was examined and T_L = 19 ˚C and T_S = 30 ˚C were obtained as a best condition. Changing the temperature allowed for control over the hole sizes.

The substrate glass was mounted on a prism to form an optically contiguous medium. A He-Ne laser operating at 632.8 nm was used in subsequent measurements and a polarizer selected for either TE- or TM-polarization. To observe the optical waveguide modes, reflectivity was measured against incident angle.

3. Results and discussion

SEM images of the fabricated samples provided sufficient evidence that cylindrical holes were etched into the 500nm-thick silica films. These through holes with a diameter of ~ 50 nm were resulted from vapor etching. Both, waveguide modes as well as the surface plasmon mode can be excited in the silica waveguide. The waveguide mode spectrum shifts when the silica waveguide film is exposed to a solution containing biotin of 500 μM. Reflectivity against incident angle in the vicinity of the TE0 mode was obtained on the as-prepared silica film before and after immersion in biotin solution. The central line shift in the as-prepared sample case was less than 0.01˚ and merely noticeable. The angular resolution in this experiment was 0.01˚. Reflectivity against angle was measured around the same mode obtained on porous silica film with a number of 1 x 10^{10} cm^{-2} holes, 500nm deep and 50 nm in diameter. The central line shift was dramatically increased up to 0.14˚. It was found that the remaining dip intensity was increased by the creation of holes and the line width was likewise increased slightly. Both observations are easily attributed to an increase of the guiding losses of the modes due to additional light scattering at the etched holes.

Angular dependent reflectivity for a TE0 mode before and after capturing streptavidin of 500 nM was also examined. For the silica waveguide before creation of pores, dip shift was estimated to be 0.06 ˚. When a number of 7 x 10^9 cm^{-2} holes were created in the silica waveguide, central position of the dip shifted dramatically by 0.53 ˚. Additional waveguides with increased hole densities were fabricated and the TE0 spectra were measured. The relationship between dip shift due to capturing of streptavidin and hole density was examined. Change in reflectivity at a constant angle ($\Delta R/R$) could be estimated from the TE0 spectra. For example, reflectivity at 53.56˚ was estimated to be 0.51 before and 0.78 after capturing of streptavidin. Based on those values, we evaluated the relative change in reflectivity ($\Delta R/R$) with respect to the unexposed sample. $\Delta R/R$ values are plotted against hole-density. It was found that the dip shift increases with number of holes. The $\Delta R/R$ value reached a maximum above 3 x 10^9 cm^{-2}. Saturation is observed, as the line width of the unexposed compared to the exposed spectra are no more overlapping. Such a shift is hardly to achieve with conventional plasmon based sensors. We expect the sensor chips to be able to detect impurities of ppb order.

4. Summary

Detection of low levels of bio-molecules with guided modes in perforated dielectric waveguides was explored. It was found that a concentration of 500 μM of biotin, which cannot be detected employing the bulk silica waveguide, could be detected with the perforated silica waveguide. Also by capturing streptavidin of 500nM, the angular position of the waveguide modes for the TE0 was shifted up to 0.53. The shifts exceed significantly the line width of the resonance itself, hence allowing for unprecedented change in the reflectivity for such low concentration of molecules to be detected. The high sensitivity of the present sensor derives from a maximization of the overlap of modal volume and the molecules to be detected via the nanometer sized holes that were created in the waveguides. The present approach will contribute significantly towards the development of ultra-high sensitive sensors in various fields.

Reference

[1] R.G.Musket, J.M.Yoshiyama, R.J.Contolini, J.D.Porter, J.Appl.Phys., **91,** 5760-5764 (2002).

---

[1] Center for Applied Near-field Optics Institute, AIST, 1-1-1 Higashi Tsukuba 305-8562, Japan

[2] Department of Electrical Engineering and Bioscience,Waseda University, Shinjuku, Tokyo 169-8555, Japan

4.10 Detection sensitivity of ERCS hydrogen analysis

T. Komatsubara, K. Sasa, S. Ishii, Y. Yamato, K. Ebisu, T. Kawamata and M. Kurosawa

In order to improve systematic error in Elastic Recoil Coincidence Spectrometry (ERCS) hydrogen analysis a new method of modification for measured sum spectrum has been developed. Stopping power for the moving proton in SiO_2 or volcanic rock can be approximated as

$$S(E) = aE^{-b}$$

as a function of the proton energy E, where a and b are fitting parameters. This approximation is rather better than the inversed linear function which was introduced in reference [1]. By using this approximation thickness from the entrance surface x can be calculated as

$$x = \frac{E_{sum}^{b+1} - E_0^{b+1} + a(b+1)2^{b+1.5}T}{a(b+1)(2^{b+1.5}-1)}$$

where E_{sum} and E_0 are sum energy and incident energy, respectively. Total thickness of the target is denoted by T in a unit of mg/cm^2. In this formula, the total thickness T and the incident energy E_0 appear explicitly. However these parameters can change only position of the spectrum, they can be replaced by an adjusting *constant* as follows.

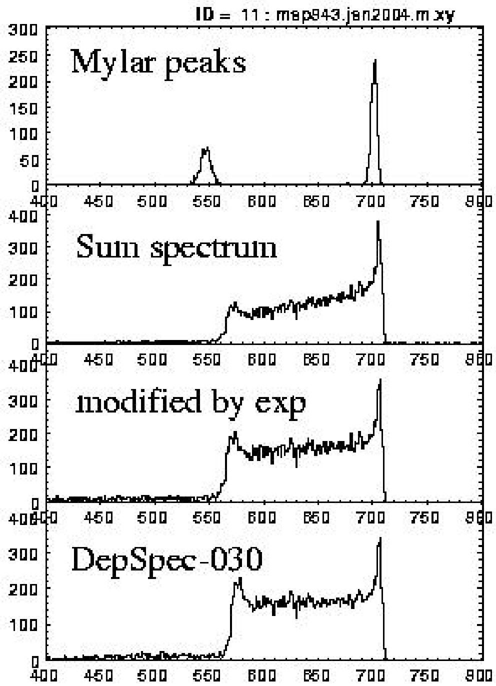

Fig. 1 Measured spectra and modified spectra. The last spectrum is hydrogen depth distribution.

$$x = \frac{E_{sum}^{b+1}}{a(b+1)(2^{b+1.5}-1)} + constant$$

By using this formula abscissa of the sum energy spectrum E_{sum} [MeV] can be converted to depth [mg/cm^2].

As an example of the calculation measured spectra and the modified spectra are shown in Fig. 1. The irradiated sample is a melt inclusion trapped by quartz gathered at Zaoh volcano. In the top spectrum, since the irradiation position is quartz part, two peaks corresponding to holding Mylar films are observed. The next spectrum is the sum energy spectrum for the melt inclusion which is large enough to penetrate host quartz. The third spectrum is a result of correction for only secondary scattering with exponential decrease, where a little incline can be observed. The last spectrum is the result of full correction of the spectrum analysis. The flat distribution is corresponding to uniformity of hydrogen concentration.

For the evaluation of the measured sensitivity of ERCS hydrogen analysis, several standard materials were irradiated.

Measured results of the hydrogen concentrations are shown in Fig. 2 compared with reference values. In this analysis hydrogen concentration of Mylar film is chosen as a reference. For the well calibrated materials of Kapton, Polyethylene, and Ti(H) the measured results by ERCS analysis agree with the calibrated values within 5% relative deviation.

The ERCS result for the lowest hydrogen density material ED-H is shown in Fig. 3 which is a glass plate sample. The measured hydrogen concentration is rather deviated from referenced value reported by FTIR measurement. Lowest limit of the ERCS hydrogen evaluation can be estimated as 1 ppm weight ration of H.

In the Fig. 3, surface contamination is clearly observed for both side of the E-DH glass. According to the hydrogen calibration, the peak intensity can be evaluated to be about 20ng/cm^2. High sensitivity of the ERCS hydrogen analysis has been appeared.

References

[1] T. Komatsubara *et al.* Nucl. Instr. and Meth. B251 (2006) 237

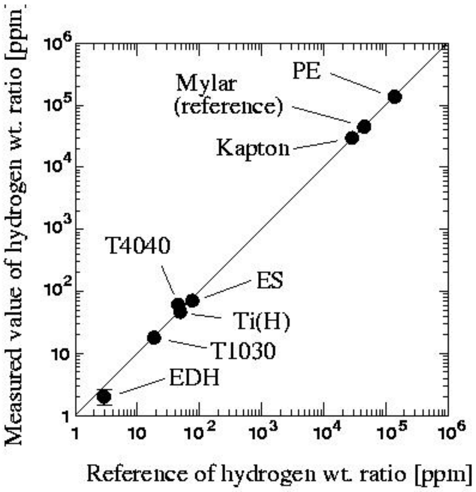

Fig. 2 Measured results of ERCS hydrogen analysis comparing to the reference values.

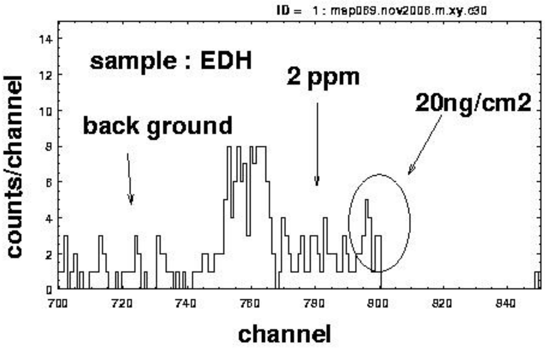

Fig. 3 Hydrogen depth distribution for the EDH sample.

5.

RELATED TOPICS

5.1 Micro on-chip pH-stat based on an irregular use of a thin-film three-electrode system

Katsuya Morimoto, Junji Fukuda, and Hiroaki Suzuki

1 INTRODUCTION

For the determination of analytes using biosensors, the detection of a pH change caused by an enzymatic reaction has been one of the very popular methods. Numerous biosensors based on the detection principle have been developed including the use of a pH-ISFET. However, a problem with this mode of operation is in that the response is affected by the buffering capacity of the analyte solution to be measured [1]. An alternative to alleviate this problem is the use of a pH-stat. A pH-stat is a device which has a function to maintain the pH of a solution in a chamber and has been used widely for acid-base titration and the determination of the activities of enzymes that accompany the hydrolysis of an analyte. However, miniaturization of the currently-used pH-stat was very difficult, because it requires an injection mechanism to enable timely injection of an accurate amount of titrant. In this study, the pH-stat was realized based on an irregular use of a thin-film three-electrode system. The mode of operation caused a negative feedback and the pH of the solution to be analyzed could be maintained at a fixed value. By measuring the electric charge generated during the feedback process, titration of an acid or a base was conducted. We also conducted the on-chip determination of urea using the pH-stat.

2 EXPERIMENTAL

Fabrication of the device

Fig. 1 shows the structure of the on-chip pH-stat. The device consisted of a polydimethylsiloxane (PDMS) compartment and a thin-film three-electrode system on a glass substrate. A pH-sensitive electrode was used for the reference electrode and was made in direct contact with an analyte solution. A Ag/AgCl electrode was used for the working electrode. The reference and auxiliary electrodes were placed in a compartment and the working electrode was placed in another compartment connected with a liquid junction. A 0.1 M KCl solution impregnated in a gel was used as an internal electrolyte for the Ag/AgCl

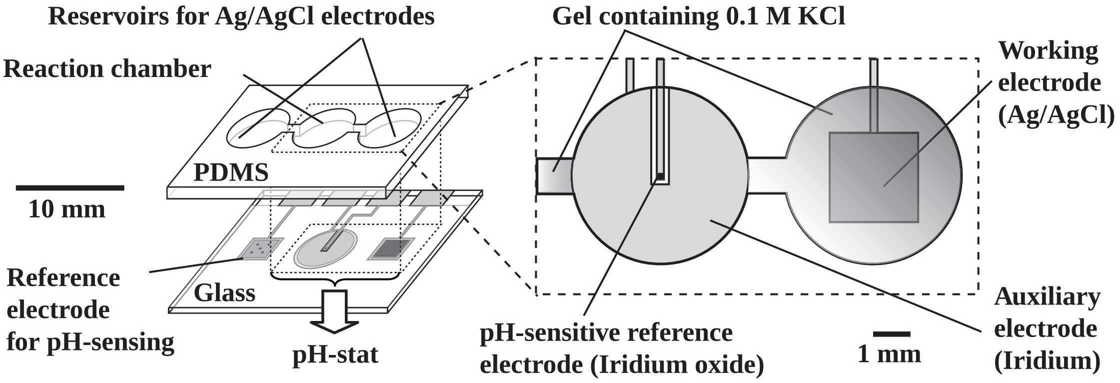

Fig. 1 Structure of the micro pH-stat.

electrodes.

Principle of operation

First, a solution of a predetermined pH is filled in the reaction chamber. The value of the resting potential of the working electrode measured with respect to the reference electrode is applied to the working electrode by using a potentiostat. When the solution pH in the reaction chamber changes, the overpotential is applied to the working electrode following the potential change of the pH-sensitive reference electrode. However, even with a very small potential shift, a large current is generated because the Ag/AgCl electrode is non-polarlizable. Accompanying this change, the electrolysis of water proceeds on the auxiliary electrode that surrounds the pH electrode. As a result, the solution pH recovers to the initial value resulting in a decrease in the overpotential. The amount of protons produced and consumed accompanying the change is related to the measured electric charge.

3 RESULTS

Fig. 2 shows a typical response curve for the pH electrode (reference electrode) in the on-chip pH-stat and the dependence of the generated charge on the concentration of acetic acid or ammonia. Linear relationships were observed between the generated charge and the concentration of acetic acid or ammonia. While the pH-stat was operating, the potential of the pH electrode recovered to the initial value immediately after a spike of pH change caused by adding an aliquot of an acetic acid solution. When the solution was added under the OFF state, no substantial change was observed in the potential of the pH electrode.

In order to demonstrate the applicability to bio-sensing, the pH-stat was used for the determination of urea. Urea is hydrolyzed by urease and the solution pH increases as ammonia is produced. Therefore, by measuring the pH change caused by the enzymatic reaction, the concentration of urea can be determined. A linear relationship was observed between the generated charge and the concentration of urea. Also, the dependence of the buffering capacity on the output was very small.

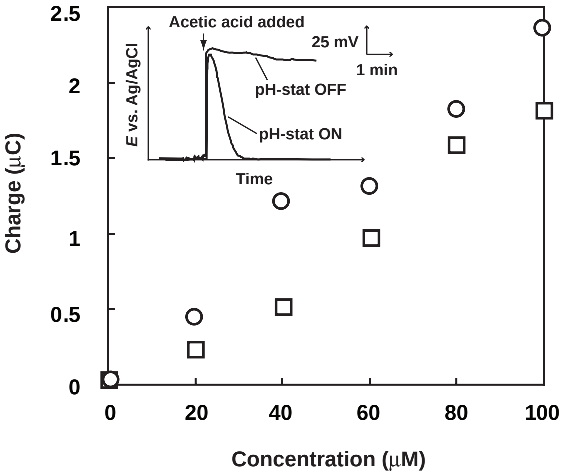

Fig. 2 Dependence of the generated charge on the concentration of acetic acid (○) and ammonia (□). Added sample volume was 0.1 μl. 10 μl of a 0.1 M sodium sulfate solution (pH 6.9, 25˚C) was used as a supporting electrolyte in the reaction chamber. The inset shows time courses of the potential of the pH electrode.

References

[1] K. Morimoto, H. Suzuki, “Micro analysis system for pH and protease activities with an integrated sample injection mechanism”, Biosensors and Bioelectronics, vol. 22, p. 86-93, 2006.

6. LIST OF PUBLICATIONS

The publications listed here are those released in the fiscal year 2006 by all the workers listed on §10.

6.1 Journals

ACCELERATOR AND EXPERIMENTAL FACILITIES

NUCLEAR PHYSICS

1. M. Yamaguchi, Y. Tagishi, Y. Aoki, T. Iizuka, T. Nagatomo, T. Shinba, N. Yoshimaru, Y. Yamato, T. Katabuchi, and M. Tanifuji, Analyzing powers of polarized deuterons in low-energy ^{6}Li(d,α)^{4}He and ^{6}Li(d,p$_0$)^{7}Li reactions in a resonance region PRC 74(2006) 064606. Published 12 December 2006 (11 pages)

2. F.Schümann, S.Typel, F.Hammache, K.Sümmerer, F.Uhlig, I.Böttcher, D.Cortina, A.Förster, M.Gai, H.Geissel, U.Greife, E.Gross, N.Iwasa, P.Koczon, B.Kohlmeyer, R.Kulessa, H.Kumagai, N.Kurz, M.Menzel, T.Motobayashi, H.Oeshler, A.Ozawa, M.Ploskon, W.Prokopowicz, E.Schwab, P.Senger, F.Strieder, C.Sturm, Zhi-Yu Sun, G.Surowka, A.Wagner, and W.Walus, Low-energy cross section of the ^{7}Be(p, γ)^{8}B solar fusion reaction from the Coulomb dissociation of ^{8}B, Physical Review C, 73, 015806 (2006).

3. A.Ozawa, Y.Z.Cai, Z.Q.Chen, M.Chiba, D.Q.Fang, Z.G.Guo, T.Izumikawa, J.X.Li, R.S.Mao, T.Ohnishi, W.Q.Shen, T.Suda, Z.Y.Sun, T.Suzuki, I.Tanihata, W.D.Tian, J.S.Wang, M.Wang, Y.B.Wei, G.Q.Xiao, Z.G.Xiao, T.Yamaguchi, Y.Yamaguchi, A.Yoshida, W.L.Zhan, H.Y.Zhang, T.Zheng, C.Zhong, Measurements of the interaction cross-sections for ^{14}Be and ^{14,15}B as projectiles with a new scheme at RIBLL, Nuclear Instruments and Methods in Physics Research B 247, 155-160 (2006).

4. A.Ozawa, K.Matsuta, T.Nagatomo, M.Mihara, K.Yamada, T.Yamaguchi, T.Ohtsubo, S.Momota, T.Izumikawa, T.Sumikama, Y.Nakashima, H.Fujiwara, S.Kumashiro, R.Matsumiya, M.Ota, D.Shinojima, H.Tanaka, T.Yasuno, S.Nakajima, T.Suzuki, K.Yoshida, K.Muranaka, T.Maemura, A.Chiba, Y.Utsuno, M.Fukuda, K.Tanaka, I.Tanihata, Y.Nojiri, T.Minamisono, J.R.Alonso, G.F.Krebs, T.J.M.Symons, Measurement of the spin and magnetic moment of ^{23}Al, Physical Review C, 74, 021301 (R) (2006).

5. T.Yamaguchi, T.Ohnishi, T.Suzuki, F.Becker, M.Fukuda, H.Geissel, M.Hosoi, R.Janik, A.Kelic, K.Kimura, S.Mandel, G.Münzenberg, S.Nakajima, T.Ohtsubo, A.Ozawa, A.Prochazka, M.Shindo, B.Sitar, P.Strmen, T.Suda, K.Sümmerer, K.Sugawara, I.Szarka, M.Takechi, A.Takisawa, and K.Tanaka, Production cross-sections of isotopes formed by fragmentation of $\sim$1 A GeV ^{80}Kr beam; Physical Review C, 74, 044608 (2006).

6. Z.Elekes, Zs.Dombradi, A.Saito, N.Aoi, H.Baba, K.Demichi, Zs.Fulop, J.Gibelin, T.Gomi, H.Hasegawa, N.Imai, M.Ishihara, H.Iwasaki, S.Kanno, S.Kawai, T.Kishida, T.Kubo, K.Kurita, Y.Matsuyama, S.Michimasa, T.Minemura, T.Motobayashi, M.Notani, T.Ohnishi, H.J.Ong, S.Ota, A.Ozawa, H.K.Sakai, H.Sakurai, S.Shimoura, E.Takeshita, S.Takeuchi, M.Tamaki, Y.Togano, K.Yamada, Y.Yanagisawa, and K.Yoneda, Proton inelastic scattering studies at the borders of the “island inversion”: The $^{3}0,31$Na and ^{33,34}Mg case, Physical Review C, 73, 044314 (2006).

7. Zs.Dombradi, Z.Elekes, A.Saito, N.Aoi, H.Baba, K.Demichi, Zs.Fulop, J.Gibelin, T.Gomi, H.Hasegawa, N.Imai, M.Ishihara, H.Iwasaki, S.Kanno, S.Kawai, T.Kishida, T.Kubo, K.Kurita, Y.Matsuyama, S.Michimasa, T.Minemura, T.Motobayashi, M.Notani, T.Ohnishi, H.J.Ong, S.Ota, A.Ozawa, H.K.Sakai, H.Sakurai, S.Shimoura, E.Takeshita, S.Takeuchi, M.Tamaki, Y.Togano, K.Yamada, Y.Yanagisawa, and K.Yoneda, Vanishing N=20 Shell Gap: Study of excited States in ^{27,28}Ne, Physical Review Letters, 96, 182501 (2006).

8. T. Kawabata, H. Akimune, H. Fujita, Y. Fujita, M. Fujiwara, K. Hara, K. Hatanaka, M. Itoh, Y. Kanada-En’yo, S. Kishi, K. Nakanishi, H. Sakaguchi, Y. Shimbara, A. Tamii, S. Terashima, M. Uchida, T. Wakasa, Y. Yasuda, H.P. Yoshida and M. Yosoi 2α+t cluster structure in ^{11}B, Physics Letters B 646, p6-11, 2007

9. B.K. Nayak, U. Garg, M. Hedden, M. Koss, T. Li, Y. Liu, P.V.Madhusudhana Rao, S. Zhu, M. Itoh, H. Sakaguchi, H. Takeda, M. Uchida, Y. Yasuda, M. Yosoi, H. Fujimura, M. Fujiwara, K. Hara, T. Kawabata, H. Akimune and M.N. Harakeh, ”Bi-modal” isoscalar giant dipole strength in ^{58}Ni, Physics Letters B 637, p43-47, 2006

10. S.Y. Wang, Y.Z. Liu, T. Komatsubara, Y.J. Ma, Y.H. Zhang, Candidate chiral doublet bands in the odd-odd nucleus Cs-126, Physical Review C 74 (1) 017302 JUL (2006)

ATOMIC AND SOLID STATE PHYSICS, AND CLUSTER SCIENCE

11. S. Tomita, J.U. Andersen, H. Cederquist, B. Concina, O. Echt, J.S. Forster, K. Hansen, B.A. Huber, P. Hvelplund, J. Jensen, B. Liu, B. Manil, L. Maunoury, S.B. Nielsen, J. Rangama, H.T. Schmidt, and H. Zettergren, “Lifetimes of C_{60}^{2-} and C_{70}^{2-} dianions in a storage ring” *J. Chem. Phys.* **124**, (2006) 024310(1-9)

12. B. Concina, P. Hvelplund, A.B. Nielsen, S. Brøndsted Nielsen, J. Rangama, B. Liu, S. Tomita, “Formation and stability of charged amino acid clusters and the role of chirality”, *J. Am. Soc. Mass Spec.* **17**, (2006) 275-279

13. H. Zettergren, P. Reinhed, K. Støchkel, H.T. Schmidt, H. Cederquist, J. Jensen, S. Tomita, S.B. Nielsen, P. Hvelplund, B. Manil, J. Rangama, B.A. Huber, “Fragmentation and ionization of C_{70} and C_{60} by slow ions of intermediate charge”, *Eur. Phys. J. D* **38**, (2006) 299-306

14. A.V. Streletskiy, P. Hvelplund, S.B. Nielsen, B. Liu, S. Tomita, A.A. Gryunkov, O.V. Boltalina, “Differences in electronic properties of fluorinated and trifluoromethylated fullerenes revealed by their propensity for dianion formation”, *J. Chem. Phys.* **124**, (2006) 144306(1-4)

15. T. Kaneko, H. Kudo, S. Tomita, R. Uchiyama, “Secondary electron emission from graphite induced by MeV/atom carbon cluster impacts”, *J. Phys. Soc. Jpn.* **75**, (2006) 034717(1-6)

16. O. Kamalou, B. Manil, J. Rangama, H. Lebius, B.A. Huber, S. Tomita, S. Broendsted Nielsen, P. Hvelplund, J. Jensen, H.T. Schmidt, H. Zettergren, H. Cederquist, “Fullerene collisions and clusers of fullerenes”, *Int. J. Mass Spectrom.* **252**, (2006) 117-125

17. B. Concina, S. Tomita, N. Takahashi, T. Kodama, S. Suzuki, K. Kikuchi, Y. Achiba, A. Gromov, J.U. Andersen, P. Hvelplund, “Delayed ionization of C_{76}”, *Int. J. Mass Spectrom.* **252**, (2006) 96-99

18. H. Kudo, W. Iwazaki, R. Uchiyama, S. Tomita, K. Shima, K. Sasa, S. Ishii, K. Narumi, H. Naramoto, Y. Saitoh, S. Yamamoto and T. Kaneko, “Energy Spectra of Electrons Induced by MeV Atom Clusters”, *Japanese Journal of Applied Physics*, **45**, No. 22, 2006, pp. L565-568.

19. S. Tomita, S. Yoda, R. Uchiyama, S. Ishii, K. Sasa, T. Kaneko, H. Kudo, “Nonadditivity of convoy- and secondary-electron yields in the forward-electron emission from thin carbon foils under irradiation of fast carbon-cluster ions”, *Phys. Rev. A* **73** (2006) 060901(R) (1-4).

20. B. Liu, P. Hvelplund, S.B. Nielsen, and S. Tomita, “Photodissociation of singly charged oligonuleotide cations: Arrhenius parameters and identification of nonstatistical processes”, *Phys. Rev. A* **74**, (2006) 052704 (1-6)

21. K. Shibata, Y. Sasaki, M. Kishimoto, H. Yanagihara, E. Kita, Magnetic Moment and Anisotropy of Iron Nitride $Fe_{16}N_2$ Nanoparticles, J. Magn. Soc, Jpn. 30, No.5, 501-504 (2006)

22. Y. Toyota, H. Yanagihara, E. Kita. Interlayer Exchange Coupling through MgO in Epitaxial Fe_3O_4/MgO/Fe(001) Trilayers, J. Magn. Soc, Jpn. 31, No.2 85-88, (2007)

23. T. Koyano T. Nomiyama, N. Kanoh, H. Numata, T. Ohba, E. Kita, H. Ohtsuka, Magnetization of α'-iron nitride produced through the fcc $\rightarrow$ bct martensitic transformation in high magnetic field, J. Appl. Phys., 100 033906-5 pages, (2006)

24. H. Yanagihara, M. Hasegawa, E. Kita, Y. Wakabayashi, H. Sawa and K. Siratori, Iron Vacancy Ordered γ-Fe_2O_3(001) Epitaxial Films: The Crystal Structure and Electrical Resistivity, J. Phys. Soc. Jpn., 75, No. 5 (2006) 054708-p5

25. Tomohiro Ikeda and Masashige Onoda, Structural and electronic properties of the triangular lattice system Na_xCoO_2, Journal of Physics: Condensed Matter **18**, 8673-8682 (2006)

26. Masashige Onoda and Tomohiro Ikeda, Modulated and unmodulated structures, and the transport mechanisms in the triangular lattice system Na_xCoO_2 with $x \simeq 0.48$, 0.58 and 0.65, Journal of Physics: Condensed Matter **19**, 186213 (14pp) (2007)

27. Kotaro Bessho, Hiroshi Matsumura, Taichi Miura, Qingbin Wang, Kazuyoshi Masumoto, Takeshi Matsuhiro, Yasuo Nagashima, Riki Seki, Tsutomu Takahashi, Kimikazu Sasa and Keisuke Sueki, AMS analysis of ^{36}Cl induced in concrete of accelerator facilities, Radiochim. Acta 94, 801-805, 2006.

28. M. Kurosawa, K. Shima, S. Ishii, K. Sasa, Trace element analysis of fused whole-rock glasses by LA-ICP-MS and PIXE, Geostandards Newsletter: The Journal of Geostandards and Geoanalysis, 30, 237-245, (2005).

29. T. Nakajima and M. Kurosawa, Rare-element mineralogy of the Uzumine granitic pegmatite, Abukuma mountains, northeastern Japan, Can. Mineral. 44, 31-44, (2006).

30. Y. Nagashima, R. Seki, T. Matsuhiro, T. Takahashi, K. Sasa, T. Usui, K. Sueki, ^{36}Cl Measurements in Japan, ”Reassessment of the Atomic Bomb Radiation Dosimetry for Hiroshima and Nagasaki-Dosimetry System 2002”, Report of the Joint US-Japan Working Group, (Japanese version), Chapter 8, Part F, pp.567-572, The Radiation Effects Research Foundation, (2006).

31. T. Komatsubara, K. Sasa, H. Ohshima, H. Kimura, Y. Tajima, T. Takahashi, S. Ishii, Y. Yamato, M. Kurosawa, K. Furuno, Hydrogen Content in Granite, ”Reassessment of the Atomic Bomb Radiation Dosimetry for Hiroshima and Nagasaki-Dosimetry System 2002”, Report of the Joint US-Japan Working Group, (Japanese version), Chapter 10, Part E, pp.764-768, Radiation Effects Research Foundation, (2006).

32. T. Komatsubara, K. Sasa, K. Okumoto, S. Ishii, Y. Yamato, K. Satou, K. Furuno, M. Kurosawa, Development of ERCS hydrogen analysis for melt inclusions in erupted magmatic samples, Nucl. Instrum. and Methods B, 251 (2006) 237-245.

33. K. Awazu, C. Rockstuhl, M. Fujimaki, N. Fukuda, J. Tominaga, T. Komatsubara, T. Ikeda, T. Ohki, High sensitivity sensors made of perforated waveguides, OPTICS EXPRESS Vol.15, No.5, 2592-2597 March (2007).

34. K. Awazu, X. Wang, M. Fujimaki, T. Komatsubara, T. Ikeda, Y. Ohki, Structure of latent tracks in rutile single crystal of titanium dioxide induced by swift heavy ions, Journal of Applied Physics 100, 044308 Aug (2006)

6.2 International conferences

1. Akira Ozawa, Reaction cross sections of unstable nuclei The sixth China-Japan Joint Nuclear Physics Symposium 2006, 5/16-20, Shanghai, China
2. I. Sugai, Y. Takeda, M. Oyaizu, H. Kawakami, S.Ishii, K. Sasa and K. Shima, First Result of Target Preparation by a HIVIPP Method in High Pressure Higher than 1 Atm, The 23rd World Conference of the International Nuclear Target Development Society (INTDS) in TSUKUBA, Japan. Tsukuba Epochal InternationalCongress Centerat Tsukuba, October 16 - 20, 2006.
3. Kimikazu Sasa, Yasuo Nagashima, Yuki Tosaki, Yuki Matsushi, Michiko Tamari, Tsutomu Takahashi, Ben Hu Zhou, Keisuke Sueki, Kotaro Bessho, Hiroshi Matsumura, Kazuho Horiuchi, Yasuyuki Shibata and Hideaki Motoyama, Preliminary results of ^{36}Cl measurement in an ice core retrieved from the Dome Fuji station by the Tsukuba AMS system, The 9th symposium of Japanese AMS society, Prospects for the New Frontiers of Earth and Environmental Sciences, 20, 21 October 2006, Takeda Hall, The University of Tokyo.
4. M. Nakazumi, H. Yanagihara and E. Kita, ”Tunnelling Magnetoresistance with NaCl Barriers”, 17P-5,19th International Colloquium on Magnetic Films and Surfaces, Sendai, August 14-18, 2006
5. Y. Toyoda, H. Yanagihara, E. Kita, T. Taniyama, ”Interlayer Exchange Coupling through Insulator in Epitaxial Fe_3-O_4/MgO/Fe Trilayers”, 15P-15, 19th International Colloquium on Magnetic Films and Surfaces, Sendai, August 14-18, 2006
6. E. Kita, K. Shibata, H. Yanagihara, Y. Sasaki, M. Kishimoto, ”Magnetic Properties of Core-Shell Type Fe16N2 Nanoparticles”, PSTh-L-420, International Magnetism ConferenceICM2006Kyoto, 2006 August
7. M. Hasegawa, H. Yanagihara, Y. Toyoda, E. Kita and L. Ranno, ”ELECTRICAL AND MAGNETIC PROPERTIES OF γ-Fe_2O_3 EPITAXIAL FILMS”, PSTu-I-356, International Magnetism ConferenceICM2006Kyoto, 2006 August

7. THESES

Ph. D. Theses

Shingo Sakai	Measurement of electron azimuthal anisotropy and implications for heavy quark flow in Au+Au collisions at $\sqrt{s_{\mathrm{NN}}}$ = 200 GeV
Tomohiro Ikeda	Crystal structures and electronic properties of the triangular lattice system $\mathrm{Na}_x\mathrm{CoO}_2$

M. Sc. Theses

Yoshimasa Ikeda	Development of Reaction Plane Detector for RHIC-PHENIX
Rei Tanabe	Measurement of Elliptic Flow of Φ-meson at $\sqrt{s_{\mathrm{NN}}}$=200GeV Cu+Cu collisions at RHIC-PHENIX
Masanori Narisawa	Performance Evaluation of Multigap Resistive Plate Chamber with a Monte Calro Simulation
Takahumi Niita	Measurements of Quantum Mechanical Two Particle Interference in $\sqrt{s_{\mathrm{NN}}}$ = 200GeV Au+Au collision at RHIC-PHENIX
Yusuke Tomita	Measurements of Directed and Elliptic Azimuthal Anisotropy in $\sqrt{s_{\mathrm{NN}}}$ = 200GeV Au+Au Collision at Extremely Forward Rapidity Region
Yuta Toyoda	Magnetic properties and electronic conduction in $\mathrm{Fe}_{3-\delta}\mathrm{O}_4$/MgO/Fe single crystal multilayers
Takuya Nishimura	Electronic energy transfer of energetic cluster ions in solids
So Yoda	Development of electrostatic ion beam trap
Yuji Kikuchi	Synthesis and the electronic properties in the triangular lattice system HCoO_2
Akira Sasaki	Crystal structure and the electronic properties in the $\mathrm{Li}_{1+x}\mathrm{V}_3\mathrm{O}_8$ insertion electrode
Hiroyuki Mishiba	Evaluation of magnetron sputtering gas aggregation cluster source with DSMC method
Toshio Sugaya	Sulfuration mechanism of gold cluster cation
Satoshi Igarashi	Developement of JAVA GUI for beam simulator MOCADI
Kanako Yamaguchi	Storage ring for mass measurement of unstable nuclei
Akira Komdo	Molecular dynamics calculation for hydrogen hydrate

8. SEMINARS

Date		Title and *Speaker*
2005		
May	10	The high baryon density CBM experiment and other QCD related research activities at the future FAIR facility in Germany *Claudia Hoehne (GSI)*
May	31	Implications for charm quark collectivity via electron measurement in Au + Au collisions at $\sqrt{s_{\mathrm{NN}}}$ = 200 GeV *Singo Sakai (Univ. of Tsukuba)*
Oct.	30	The role of Ions in Particle Nucleation *Jens Olaf Pepke Pedersen (Danish National Space Center)*
Nov.	22	The AMS measurement and it's application in CIAE *He Ming (CIAE)*
Dec.	13	Development of Reaction Plane Detector for RHIC-PHENIX *Yoshimasa Ikeda (Univ. of Tsukuba)*
Dec.	20	Measurement of Elliptic Flow of Φ-meson at $\sqrt{s_{\mathrm{NN}}}$=200GeV Cu+Cu collisions at RHIC-PHENIX *Rei Tanabe (Univ. of Tsukuba)*
Dec.	20	Evaluation of magnetron sputtering gas aggregation cluster source with DSMC method *Hiroyuki Mishiba (Univ. of Tsukuba)*
Dec.	27	Measurement of electron azimuthal anisotropy and implications for heavy quark flow in Au+Au collisions at $\sqrt{s_{\mathrm{NN}}}$ = 200 GeV *Shingo Sakai (Univ. of Tsukuba)*

2007

Jan. 10 Performance Evaluation of Multigap Resistive Plate Chamber with
a Monte Calro Simulation
Masanori Narisawa (Univ. of Tsukuba)

Jan. 10 Sulfuration mechanism of gold cluster cation
Toshio Sugaya (Univ. of Tsukuba)

Jan. 17 Developement of JAVA GUI for beam simulator MOCADI
Satoshi Igarashi (Univ. of Tsukuba)

Jan. 24 Measurements of Quantum Mechanical Two Particle Interference
in $\sqrt{s_{\mathrm{NN}}}$ = 200GeV Au+Au collision at RHIC-PHENIX
Takahumi Niita (Univ. of Tsukuba)

Jan. 24 Storage ring for mass measurement of unstable nuclei
Kanako Yamaguchi (Univ. of Tsukuba)

Feb. 31 Measurements of Directed and Elliptic Azimuthal Anisotropy in
$\sqrt{s_{\mathrm{NN}}}$ = 200GeV Au+Au Collision at Extremely Forward Rapidity Region
Yusuke Tomita (Univ. of Tsukuba)

Feb. 31 Molecular dynamics calculation for hydrogen hydrate
Akira Kondo (Univ. of Tsukuba)

March 1 Molecular wave function can not be expressed by atomic wave fucntion
Yoshiyuki Kawazoe (Tohoku Univ.)

9. SYMPOSIA

Progress of nuclear reaction analysis

24 November, 2006
Room C305, Tandem Accelerator Complex,
Research Facility Center for Science and Technology, University of Tsukuba

1. Oppenheimer-Phillips process with CDCC method : *Y. Aoki (Univ. of Tsukuba)*
2. Sub-Coulomb barrier effect of ^{118}Sn(d,p) reaction : *M. Iijima (Univ. of Tsukuba)*
3. Review and perspectives of Continuum-Discretized Coupled Channel method : *K. Ogata (Kyushu Univ.)*
4. Nonlocal folding optical potential : *Y. Iseri (Chiba Keizai College)*
5. Nuclear reaction study for astrophysics : *S. Kubono (CNS)*
6. Theoretical study for low energy reactions, ^{6}Li(d,p$_0$)^{7}Li and ^{6}Li(d,α)^{4}He : *M. Tanifuji (Hosei Univ.)*
7. Resonant states in a nuclear reaction : *K. Kato (Hokkaido Univ.)*
8. Nuclear reaction and computer science : *K. Yabana (Univ. of Tsukuba)*
9. Deuteron breakup and charge exchange reaction : *H. Okamura (Nagano National College of Technology)*

New evolution toward to an interdisciplinary use of the heavy ion beams produced by a multi tandem accelerator system -Tendency and Results of the UTTAC Research Works-

16 March, 2007

Room C305, Tandem Accelerator Complex,
Research Facility Center for Science and Technology, University of Tsukuba

1. The UTTAC middle term objectives and research plans : *Y. Nagashima (Univ. of Tsukuba)*
2. Status of the Tsukuba AMS system and ^{36}Cl measurements of the Fuji dome ice core sample at the Antarctica : *K. Sasa (Univ. of Tsukuba)*
3. Measurements of ^{10}Be and ^{26}Al in the old environmental samples -As a search of an index for study of a fluctuation of comic ray intensity or dating- : *K. Horiuchi (Hirosaki Univ.)*
4. The assessment for thermal neutron radiation on a concrete shielding of an accelerator facility by mean of ^{36}Cl-AMS measurement : *K. Bessho (KEK)*
5. Study of the fluid inclusions in a granite sample by mean of PIXE measurement : *M. Kurosawa (Univ. of Tsukuba)*
6. Reassessment of the Atomic Bomb Radiation Dosimetry for Hiroshima and Nagasaki -Dosimetry System 2002- : *M. Hoshi (Hiroshima Univ.)*
7. Status report of hydrogen analysis by proton-proton elastic recoil coincidence spectrometry : *T. Komatsubara (Univ. of Tsukuba)*
8. Status of nuclear studies and future plans at UTTAC : *A. Ozawa (Univ. of Tsukuba)*
9. Basic and application physics with re-accelerated short lived radio isotope beam : *H. Miyatake (KEK)*
10. Application to a nano-photonics field at the UTTAC : *K. Awazu (National Institute of Advanced Industrial Science and Technology)*
11. A challenge to a world record stripper foil with an ultra-super long life time in a charge exchange use : *I. Sugai (KEK)*
12. A study of a solid electron excitation process by an irradiation of a high energy cluster ion : *S. Tomita (Univ. of Tsukuba)*
13. Interdisciplinary approaches by an accelerated ion beam : *H. Kudo (Univ. of Tsukuba)*

10. LIST OF PERSONNEL

Tandem Accelerator Complex

Y. Nagashima	Director, Professor
T. Komatsubara	Assistant Professor
K. Sasa	Assistant Professor
S. Ishii	Mechanical Engineer
H. Kimura	Computer Engineer
H. Oshima	Electric Engineer
Y. Tajima	Mechanical Engineer
T. Takahashi	Electric Engineer
Y. Yamato	Electric Engineer
Y. Matsushi	Research Fellow
Y. Tagishi	Technical Assistant
M. Moro	Administrative Stuff

Research Members

Inst. of Physics

Y. Aoki
I. Arai
T. Chujo
S. Esumi
S. Katoh
T. Komatsubara
Y. Miake
M. Onoda
A. Ozawa
K. Sasa
Y. Yasuda

Inst. of Applied Physics

K. Akimoto
E. Kita
H. Kudo
T. Makimura
N. Tomita
A. Uedono
H. Yanagihara

Inst. of Material Science

J. Fukuda
H. Ikeda
T. Koyano
H. Mizubayashi
H. Suzuki
H. Tanimoto

Inst. of Geoscience

M. Kurosawa
N. Tase

Inst. of Chemistry

K. Sueki

Inst. of Basic Medical Science

Y. Nagashima

Graduate Students

Doctoral Degree Programs of Pure and Applied Science

H. Arai
Zhou Benhu
M. Hashimoto
M. Iijima
M. Konno
M. Kubo
H. Masui
K. Miki
M. Nakazumi
M. Oka
J. Sawahata
J.W. Seo
M. Shimomura
K. Takao
H. Tokano
N. Yagi

Master's Degree Programs of Pure and Applied Science

T. Ebisawa
K. Ebisu
J. Hagiwara
Y. Hashizume
T. Hoya
S. Igarashi
Y. Ikeda
T. Ishikawa
K. Ito
S. Kanda
H. Kasai
Y. Kikuchi
A. Kondo
T. Maekoya
K. Miki
M. Minakawa
H. Mishiba
Y. Mizuguchi
M. Narisawa
T. Niida
T. Nishimura
T. Moriguchi
Y. Odajima
K. Okumoto
W. Onoda
A. Sasaki
T. Sato
T. Sugaya
T. Takahashi
Y. Toyota
R. Tanabe
Y. Tomita
Y. Toyota
K. Watanabe
S. Yoda
D. Yoshioka

Master's Degree Programs of Education

T. Kawamata
K. Yamaguchi

Doctoral Degree Programs of Life and Environmental Sciences

Y. Tosaki

Undergraduates

H. Aizawa
S. Amano
M. Fujieda
H. Funagi
I. Goto
R. Inaba
D. Inomata
M. Murakami
Y. Saito
D. Sakata
M. Sano
Y. Sato
N. Seya
N. Shiobara
T. Suzuki
Y. Suzuki
S. Takahashi
M. Tamari
S. Tsunegi
A. Onishi
N. Onishi
T. Waki
K. Yamada
S. Yamaguchi

Scientific Guests and Fellows

K. Awazu	AIST
M. Fujimaki	AIST
T. Ikeda	Waseda Univ.
S.J. Yu	Waseda Univ.
H. Aiba	Waseda Univ.
K. Sugimoto	Waseda Univ.
Y. Koganezawa	Waseda Univ.
J. Watanabe	Tokyo Univ.
T. Miura	KEK
K. Bessho	KEK
H. Matsumura	KEK
K. Masumoto	KEK
I. Sugai	KEK
Y. Takeda	KEK
M. Oyaizu	KEK
H. Kawakami	KEK
T. Hayakawa	JAEA
T. Shizuma	JAEA
T. Ohura	Tokyo Metropolitan Univ.
M. Yamazaki	Tokyo Metropolitan Univ.
H. Hashizume	Tokyo Metropolitan Univ.
M. Ebihara	Tokyo Metropolitan Univ.
J. Asai	RIKEN
R. Ichimiya	RIKEN
K. Kurita	Rikkyo Univ.
M. Kawashima	Rikkyo Univ.
K. Sakashita	Tokyo Institute of Technology
N. Okumura	Nagano College of Technology